Journal of Materials Chemistry A

ROYAL SOCIETY OF CHEMISTRY

PAPER

View Article Online
View Journal | View Issue

Cite this: J. Mater. Chem. A, 2026, 14, 15119

Structural origins of photocatalytic properties in Ruddlesden–Popper $Sr_{n+1}Ti_nO_{3n+1}$ ($n = 1, 2$) and their topochemically fluorinated phases $Sr_{n+1}Ti_nO_{(3n+1)-x}F_{2x}$ ($x \approx n$)

Shama Perween, *[a] Kevin Matthias Ries, [b] Anja Hofmann, [b] Tommi Hendrik Aalto, [a] Harol Moreno Fernández, [c] Marc Widenmeyer, [d] Robert Löser, [e] Jana Timm, [b] Guido Schmitz, [e] Petia Atanasova, [f] Jan Philipp Hofmann, [c] Oliver Clemens, [a] Roland Marschall [b] and Chengchao Zhong [g]

We present a comparative study of $n = 1$ and $n = 2$ Ruddlesden–Popper (RP) titanates Sr_2TiO_4 and $Sr_3Ti_2O_7$, as well as their oxyfluorides $Sr_2TiO_3F_2$ and $Sr_3Ti_2O_5F_4$, synthesized *via* low-temperature topochemical fluorination to study structure–property relationships in photocatalytic hydrogen (H_2) evolution. In Sr_2TiO_4, fluorination lowers the symmetry from *I*4/*mmm* to *P*4/*nmm*, placing Ti in a locally non-centrosymmetric site and producing ordered, asymmetric TiO_5F units. By contrast, $Sr_3Ti_2O_7$ retains its tetragonal *I*4/*mmm* symmetry upon fluorination with Ti remaining in a locally non-centrosymmetric environment. Photocatalytic H_2 evolution shows a ~6.3-fold enhancement for $Sr_2TiO_3F_2$ compared to Sr_2TiO_4, which might be attributed to inversion symmetry breaking and the resulting internal local dipole fields that promote charge separation. In contrast, $Sr_3Ti_2O_7$ exhibits much higher intrinsic activity than Sr_2TiO_4 (~30-fold), likely governed by dimensionality, while its fluorinated phase $Sr_3Ti_2O_5F_4$ shows suppressed performance due to the absence of local polarity, which limits beneficial fluorination effects and diminishes charge-separation efficiency, as supported by transient absorption spectroscopy (TAS) results. TAS reveals distinct charge-carrier dynamics, with $Sr_3Ti_2O_7$ showing the highest photogenerated electron population and $Sr_2TiO_3F_2$ exhibiting enhanced long-lived electrons, consistent with improved charge separation. Density functional theory (DFT) calculations show that fluorination deepens the O 2p valence band, slightly raises the Ti 3d conduction edge, and reduces *c*-axis dispersion, consistent with the UV-Vis and Butler–Ginley analyses. The resulting increase in electron effective mass suppresses charge mobility along the *c*-axis, lowering conduction dimensionality. These findings establish anion sublattice engineering as a selective route to tune local symmetry, charge-carrier dynamics, and photocatalytic performance in RP-type titanates.

Received 22nd October 2025
Accepted 23rd February 2026

DOI: 10.1039/d5ta08602g

rsc.li/materials-a

1 Introduction

The global transition toward sustainable energy has brought hydrogen (H_2) into focus as a potential energy carrier. Among the various strategies for H_2 production, photocatalytic water splitting offers a direct and environmentally benign route to convert solar energy into chemical energy, with no intrinsic carbon dioxide (CO_2) emissions.[1] At the core of this process lies the challenge of developing semiconductor photocatalysts capable of efficient light

[a]University of Stuttgart, Institute of Materials Science, Chemical Materials Synthesis, Heisenbergstraße 3, 70569 Stuttgart, Germany. E-mail: shama.perween@imw.uni-stuttgart.de; Tel: +49 711 685 61937

[b]Department of Chemistry, Chair of Physical Chemistry III, University of Bayreuth, Universitätsstraße 30, 95447 Bayreuth, Germany

[c]Technical University of Darmstadt, Department of Materials and Geosciences, Surface Science Laboratory, Peter-Grünberg-Straße 4, 64287 Darmstadt, Germany

[d]Technical University of Darmstadt, Department of Materials and Geosciences, Research Division of Materials & Resources, Peter-Grünberg-Straße 2, 64287 Darmstadt, Germany

[e]University of Stuttgart, Institute of Materials Science, Materials Physics, Heisenbergstraße 3, 70569 Stuttgart, Germany

[f]University of Stuttgart, Institute of Materials Science, Bioinspired Materials, Heisenbergstraße 3, 70569 Stuttgart, Germany

[g]Ritsumeikan University, Graduate School of Life Sciences, 1-1-1 Noji-higashi, Kusatsu, Shiga 525-8577, Japan

absorption, charge-carrier generation, and catalytic redox activity at the catalyst–reactant interface.[2–4]

Titanium-based perovskite oxides are among the most studied photocatalysts for H_2 evolution, owing to their chemical stability and typical non-toxicity, provided that the A-site does not contain hazardous cations such as lead (Pb). Their suitable conduction band (CB) positions for proton (H^+) reduction, with activity further enhanced through doping, defect control, nanoscale engineering, and co-catalyst loading.[5–10] Beyond simple ABO_3 perovskites, layered perovskite-related oxides have attracted increasing attention for photocatalysis because their structural anisotropy, inherent interstitial sites, and compositional flexibility allow fine-tuning of structural, optical, and electronic properties.[11–14] Among these, the Ruddlesden–Popper (RP) phases, with general formula $A_{n+1}B_nO_{3n+1}$, have attracted considerable interest. They are constructed from perovskite-like ABO_3 blocks periodically separated by rock-salt AO layers, where the integer n determines the thickness of the perovskite block and thus the dimensionality of the electronic and transport properties.[15] The layered topology of RP phases, with a maximum tetragonal symmetry ($I4/mmm$, space group 139), includes at least three crystallographically distinct anion (X) sites, *e.g.*, for $n = 1$: equatorial ($X1$, 4*c*), apical ($X2$, 4*e*), and interstitial ($X3$, 4*d*). In contrast, for $n = 2$, the doubling of the perovskite slab introduces two inequivalent apical positions: one facing the rock-salt AO layer and the other within the perovskite bilayer, equatorial ($X1$, 8*g*), apical central ($X2$, 4*e*), apical terminal ($X3$, 4*e*), and interlayer ($X4$, 4*c*) within the AO layers, which provides dimensional control, anisotropic transport pathways, and broad tolerance for structural distortions and chemical substitutions, making them a versatile platform for structure–property engineering.[16] This multiplicity of apical sites provides further flexibility for anion substitution and defect accommodation upon topochemical modification. These characteristics enable the incorporation or substitution of additional anions, such as fluoride, into interstitial sites to form mixed-anion compounds.[17–28]

Recent advances in mixed-anion chemistry highlight low-temperature topochemical fluorination as a powerful strategy to modulate symmetry and electronic states, thereby enhancing charge separation and photocatalytic performance in layered perovskite oxides.[29–34] The layered RP framework, with its distinct anion sites, can accommodate mixed-anion substitution that alters local coordination and drives symmetry lowering.[32,35–46] This structural flexibility enables fluorination to induce local polarity, which facilitates more effective charge separation and improves photocatalytic activity. This local polarity facilitates more effective charge separation, thereby improving photocatalytic activity. Polarity-driven enhancements have been reported in perovskite and layered oxyhalide systems,[32,36–42,47,48] where topochemical fluorination has induced pronounced local polar distortions, underscoring the broader potential of mixed-anion chemistry to tailor structural symmetry and functional properties.[47] However, these effects have not been systematically established for RP-type titanates, while various strategies such as cation substitution and heterostructure formation have been explored to enhance the activity of layered titanates, reports on anion modification, especially fluorination, remain scarce, particularly for higher homologues. Prior studies have indicated that fluorine incorporation can generate internal fields that aid carrier separation. For example, Yu and Xu[49] fluorinated Cr-doped Sr_2TiO_4 to $Sr_2Ti_{0.095}Cr_{0.05}O_3F_2$ and observed enhanced visible-light H_2 evolution, which they attributed to uneven F ordering that creates a built-in electric field across the RP layers. Furthermore, Jeong *et al.*,[50] reported that the RP-type photocatalyst $NiO/Sr_3Ti_2O_7$ achieves overall water splitting, with activity strongly dependent on the NiO loading method. Furthermore, recent work on fluorine-enabled anion substitution in layered perovskites, such as the F-expedited nitridation of Sr_2TiO_4 using the oxyfluoride precursor $Sr_2TiO_3F_2$ ($n = 1$), demonstrated that this approach enables higher nitrogen (N) incorporation and suppresses Ti^{3+}/oxygen-vacancy defects, thereby improving charge separation and water-splitting performance.[20]

In this present study, we investigate the influence of topochemical fluorination in RP-type titanates, $Sr_{n+1}Ti_nO_{3n+1}$, on their corresponding oxyfluorides, $Sr_{n+1}Ti_nO_{(3n+1)-x}F_{2x}$ ($n = 1$ and 2; x determined by the molar amount of polyvinylidene fluoride (PVDF)), focusing on their structure-dependent properties in the context of photocatalytic H_2 evolution, which has not been previously addressed. Our results show that fluorination predominantly governs structural symmetry and photocatalytic activity, while having minimal influence on optical band gaps or surface morphologies.

Shama Perween

Shama Perween received her PhD in Materials Science and Engineering from RGIPT, India, in 2019. She established her independent research career at the University of Stuttgart with competitive funding from the German Research Foundation (DFG). Her research addresses photocatalytic hydrogen evolution, contributing to the development of sustainable hydrogen technologies for clean energy conversion and storage. She investigates topochemical anion exchange to tune crystal structure and optical–electronic properties in layered mixed-anion systems. She is actively involved in international scientific societies, including the American Ceramic Society (ACerS), co-organizes symposia, and contributes to science outreach initiatives in Baden-Württemberg promoting sustainable energy materials research.

2 Experimental

2.1 Synthesis of oxides and oxyfluorides

The RP oxide phases, $n = 1$ and 2 ($Sr_2TiO_4/Sr_3Ti_2O_7$), were synthesized by using a solid-state reaction method as reported earlier.[51–54] In this method, precursors of TiO_2 (Anatase, Alfa

Aesar, 99.9%) and $SrCO_3$ (Alfa Aesar, 99%) were dried at 500 °C for 2 h. Stoichiometric amounts of the starting materials, calculated to yield 5 g of product, were mixed in a 50 mL ZrO_2 jar containing ten 10 mm ZrO_2 balls using a planetary ball mill (Retsch PM 200 – a VERDER Company) at 500 rpm for 1 h, and calcined twice at 1250 °C for 24 h in air with an intermediate hand-milling step; heating and cooling rates of 2 °C min^{-1} were used. For the synthesis of $Sr_3Ti_2O_7$ ($n = 2$), a 3 wt% excess of TiO_2 was used. For the topochemical fluorination of $Sr_{n+1}Ti_nO_{3n+1}$ ($n = 1$ and 2; also in this present study, $n \approx x$) to $Sr_{n+1}Ti_nO_{(3n+1)-x}F_{2x}$, the oxide was hand-milled together with the fluorinating agent poly(vinylidene fluoride) $(CH_2CF_2)_m$, m represents monomer units, (PVDF; Sigma-Aldrich) with the molar ratio of $1/m$ $(CH_2CF_2)_m$ to $Sr_2TiO_4/Sr_3Ti_2O_7$ being 1.05 : 1 and 2.1 : 1, respectively (*i.e.*, a 5% excess), and heated to 370 °C for 24 h applying heating and cooling rates of 2 °C min^{-1} under an air atmosphere.[34,54] The corresponding reaction equations are given in eqn (1) and (2), respectively.

$$Sr_2TiO_4 + 1/m(CH_2CF_2)_{m=1} + 2O_2 \xrightarrow{\Delta T} Sr_2TiO_3F_2 + 2CO_2\uparrow + H_2O\uparrow \quad (1)$$

$$Sr_3Ti_2O_7 + 2/m(CH_2CF_2)_{m=1} + 4O_2 \xrightarrow{\Delta T} Sr_3Ti_2O_5F_4 + 4CO_2\uparrow + 2H_2O\uparrow \quad (2)$$

2.2 Characterization

2.2.1 Powder X-ray diffraction (PXRD) and Rietveld refinements. PXRD patterns were collected using a Rigaku SmartLab diffractometer in Bragg–Brentano geometry with a Cu-K_α source ($K_{\alpha1}$ and $K_{\alpha2}$ with an intensity ratio of 2 : 1) and a HyPix-3000 detector, without a monochromator. Data were recorded over an angular range of 2θ from 5° to 130°, with a step size of 0.005° and a scan speed of $1^\circ \cdot min^{-1}$. Analysis of diffraction data was performed using the Rietveld method with the program TOPASV6.0 (ref. 55 and 56) covering the entire 2θ range. The instrumental intensity distribution was determined using a reference scan of LaB_6 (NIST 660a). The microstructural parameters (crystallite size and strain broadening) were refined to adjust the peak shapes. Thermal displacement parameters were constrained to be the same for all atoms of all phases to minimize quantification errors and correlation with occupancy parameters.

To evaluate the structural stability of the RP-type oxides and oxyfluorides in aqueous environments, PXRD measurements were performed on Sr_2TiO_4, $Sr_2TiO_3F_2$, $Sr_3Ti_2O_7$, and $Sr_3Ti_2O_5F_4$ after dispersing the samples in water (1 mg mL^{-1}) and allowing them to soak for 24 h under ambient conditions. For this, the aqueous slurries of the materials were drop-cast onto low-background, single-crystalline Si wafer XRD substrates, and measurements were performed under wet conditions. The structural models for the oxides Sr_2TiO_4 ($n = 1$, tetragonal, *I*4/*mmm*, ICSD Collection Code: 20293) and $Sr_3Ti_2O_7$ ($n = 2$, tetragonal, *I*4/*mmm*, ICSD Collection Code: 20294) as well as their oxyfluorides $Sr_2TiO_3F_2$ ($n = 1$, tetragonal, *P*4/*nmm*, ICSD Collection Code: 95266) and $Sr_3Ti_2O_5F_4$ ($n = 2$, tetragonal, *I*4/*mmm*, ICSD Collection Code: 141713) were adopted from the ICSD database and used as starting models for Rietveld analysis of the XRD data.

In addition, all the samples were characterized by PXRD after photocatalytic hydrogen evolution to assess phase stability following photocatalytic performance, using a Malvern PANalytical Empyrean XPert Pro device equipped with a PIXcel 1D detector generating Cu-K_α irradiation ($\lambda_1 = 1.5406$ Å; $\lambda_2 = 1.54443$ Å) using an emission current of 40 mA and an acceleration voltage of 40 kV. Measurements were carried out with a scattering slit of 1°, a step size of 0.0660°, and a scan step time of 151.7250 s.

2.2.2 UV-visible diffuse reflectance spectroscopy. Ultraviolet-visible diffuse reflectance spectroscopy (UV-Vis DRS) data of the synthesized compounds were recorded at room temperature over a wavelength range of 240–2000 nm (5.2–0.6 eV) using a J&M TIDAS UV-Vis-NIR spectrophotometer equipped with a reflection measuring head. A $BaSO_4$ standard was used as a reference. The optical response was assessed by calculating apparent absorbance as:

$$A = -\log(R) \quad (3)$$

where A is the absorbance and R is the reflectance, and by plotting the Kubelka–Munk (K–M) function $F(R_\infty)$ directly against wavelength. The optical band gaps of the samples were estimated using the K–M function,[57] which transforms diffuse reflectance data into absorbance-like values suitable for powdered samples.[58] The reflectance of an optically thick sample (R_∞) was converted using the relation:

$$F(R_\infty) = (1 - R_\infty)^2/(2R_\infty) \quad (4)$$

where $F(R_\infty)$ approximates the absorbance. In this study, band gaps were determined by plotting photon energy ($h\nu$) directly against the Kubelka–Munk absorbance function $F(R_\infty)$, *i.e.*, an 'energy *vs.* absorbance' plot, and estimating the onset of absorption from the inflection point or linear rise in the curve.

2.2.2.1 Butler–Ginley electronegativity approach for band-edge estimation. Band positions were estimated from the UV-Vis DRS optical gaps using the Butler–Ginley approach.[59–62] The elemental Mulliken (absolute) electronegativity for each constituent, χ_i (eV), was obtained from tabulated ionization energies (IEs) and electron affinities (EAs) using tabulated datasets[63–65] *via* the following equation:

$$\chi_i = \frac{1}{2}(IE_i + EA_i) \quad (5)$$

The averaged Mulliken electronegativity of the formula unit, $\bar{\chi}$ (eV), was evaluated as the stoichiometric geometric mean of the absolute Mulliken electronegativities (in eV) of the constituent elements as follows:

$$\bar{\chi} = \left(\prod_i \chi_i^{n_i}\right)^{1/\sum_i n_i} \quad (6)$$

where n_i is the number of atoms of element i in the formula unit. The conduction and valence band edge positions of the RP oxides and oxyfluorides were estimated using the Butler–Ginley electronegativity method,[59–65] while the experimentally derived optical band gaps (E_g) from UV-Vis DRS were used as input parameters, which can be calculated as:

$$E_{CB} = \bar{\chi} - E_e - \tfrac{1}{2} E_g \quad (7)$$

The valence/conduction band edge relative to the normal hydrogen electrode (NHE) was obtained from the following equation:

$$E_{VB} = E_{CB} + E_g \quad (8)$$

where E_{CB} and E_{VB} stand for the conduction band edge potential and valence band edge potential, respectively, and E_e refers to the energy of free electrons on the hydrogen scale ($E_e = 4.5$ eV). Band edges are reported *vs.* NHE (Butler–Ginley). To account for the solution conditions, these values were further converted to the reversible hydrogen electrode (RHE) scale at the relevant pH (=7.0) and the factor 0.059 at 25 °C, as derived from the Nernst equation, as follows:

$$E_{(RHE)} = E_{(NHE)} - 0.059\ \text{pH} \quad (9)$$

For all calculations we used a single, consistent elemental χ dataset (Mulliken absolute scale, in eV): Sr = 2.87 eV, Ti = 3.45 eV, O = 7.54 eV, and F = 10.40 eV.[63–65] This semi-empirical procedure typically carries an uncertainty of ~0.2–0.3 eV.[66] Additionally, for comparison with our earlier RP-type indate oxide/oxyfluoride system ($LaBaInO_4$/$LaBaInO_3F_2$),[33] we applied the same protocol using the same dataset, La = 3.07 eV, Ba = 2.68 eV, In = 3.09 eV, O = 7.54 eV, F = 10.41 eV,[63–65] and the corresponding $\bar{\chi}$ values with E_{CB} and E_{VB} are calculated.

2.2.3 Transient absorption spectroscopy (TAS). Transient absorption spectroscopy data were recorded with an LP980 spectrometer (Edinburgh Instruments) in diffuse reflectance geometry. Prior to the measurements, the powder samples were filled in a quartz cuvette in each case, flushed with argon (Ar), and sealed gas-tight with parafilm. The pump laser pulse excitation was set to 355 nm (Nd:YAG laser produced by Ekspla, NT340). A 150 W Xenon arc lamp was used as the probe pulse. The decays were fitted with mono- or biexponential decay functions using Origin 2019. Furthermore, due to the increased baseline in the TAS decays the fitting for the biexponential was first performed in the range between 0 and 150 ns with a monoexponential decay function, and afterward the received values were implemented in the biexponential decay fitting for the whole range (0 to 2500 ns).

2.2.4 Scanning electron microscopy (SEM). To see the morphological features of oxides and their oxyfluorides, SEM images were taken. The SEM, equipped with a secondary electron detector, was operated on an FEI SCIOS dual beam instrument operated at an accelerating voltage of 30 keV. The powder samples were deposited on carbon tape. To prevent surface charging during imaging, a thin gold coating of approximately 10 nm was sputtered onto all samples prior to measurement.

2.2.5 Brunauer–Emmett–Teller (BET) surface area measurements. Nitrogen (N_2) physisorption measurements were performed to analyze the surface area of the materials synthesized. The adsorption and desorption isotherms were recorded using an Autosorb iQ from Quantachrome Instruments. Before the measurements, approximately 700 mg of the samples were heated up to 350 °C under vacuum and were outgassed for 7 h. Afterwards, the N_2 physisorption measurements were performed in a liquid N_2 bath at −196 °C. From the adsorption isotherms, the surface areas were calculated using the Brunauer–Emmett–Teller (BET) method.

2.2.6 X-ray photoelectron spectroscopy. To determine the oxidation states of the oxyfluorides relative to their parent oxides, we performed X-ray photoelectron spectroscopy (XPS) using a Thermo Fisher Escalab 250 spectrometer implemented at the DAISY-SOL cluster tool. It is equipped with an Al K_α X-ray source (monochromatic Thermo Fisher XR6, $h\nu$ = 1486.74 eV). Survey and high-resolution spectra were measured in fixed analyzer transmission mode with a pass energy of 50 eV (step size of 0.5 eV) for the survey and 20 eV (step size of 0.05 eV) for the core levels. The system was calibrated to the 0.00 eV binding energy of the Fermi level of sputter-cleaned Ag, as well as to the emission lines of Au $4f_{7/2}$ at 83.98 eV, Ag $3d_{5/2}$ at 368.26 eV, and Cu $2p_{3/2}$ at 932.67 eV binding energy with deviations ≤0.1 eV. Charge compensation during XPS measurements was achieved using a flood gun, with the voltage carefully tuned to minimize differential charging. Energy calibration was carried out using the C 1s and O 1s reference peaks. The data analysis was performed with CasaXPS, version 2.3.18.[67] Because charge compensation was applied using a flood gun, the sample potential was not rigidly coupled to the spectrometer ground. Consequently, absolute energy referencing to the Fermi level or determination of the valence band maximum was not considered reliable. Instead, spectra were calibrated using the C 1s (285 eV) and O 1s peaks as internal references. The Ti 2p core-level spectra were fitted using a Shirley background and Lorentzian-asymmetric (LA (1.53,243)) line shapes. The Ti $2p_{3/2}$ and Ti $2p_{1/2}$ components were constrained by a spin–orbit splitting of 5.7 eV and an area ratio of 2 : 1, consistent with the expected spin–orbit coupling of Ti 2p states. The full-width at half maximum (FWHM) values were kept within physically reasonable limits for each chemical state. Quantification was carried out using Scofield photoionization cross-sections.[68]

2.2.7 Experimental evaluation of photocatalytic hydrogen evolution. Photocatalytic H_2 evolution experiments were performed with all oxides and their respective oxyfluorides to investigate the photocatalytic activities. For this purpose, 40 mg powder samples of each compound (freshly synthesized) were dispersed in a mixture of 550 mL of ultrapure water system A 32 (VWR) and 50 mL of ethanol (VWR Chemicals), and then ultrasonicated for 10 min before being filled into the reactor. Before irradiation, the dispersion was cooled and maintained at a temperature of 10 °C (Lauda Proline RP845) using a double-walled glass reactor, and flushed with Ar (99.999% purity) at a gas flow of 100 mL min^{-1} (Bronkhorst El-Flow Select) to remove all air. A double-walled borosilicate inlet was used to

house the lamp, blocking all wavelengths below 250 nm. A noncontinuous iron-doped Hg light source with 500 W power was used as an immersion lamp (TQ718-Z4 Peschl Ultraviolet). The samples were stirred during the reaction process. Gas evolution was measured using a quadrupole mass spectrometer (HPR-20 Q/C Hiden Analytical), with one data point being collected approximately every 60 seconds. An aqueous solution of H_2PtCl_6 (Carl Roth, 99.995%) was added through a septum without exposing the reactor to air, using a syringe, before the lamp was started, resulting in *in situ* photo-deposition of Pt as a 0.1 wt% co-catalyst onto the surface of the materials within the first seconds of irradiation. The lamp was switched off after 2 hours. A schematic representation and a corresponding photograph of the immersion-lamp photocatalytic reactor used in the laboratory are provided in the SI Fig. S1. Note that mercury light consists of several spikes at different wavelengths and is not a continuous light source, as compared to Xe light (see SI, Fig. S2). Photocatalytic activity is therefore evaluated and discussed for all the samples in terms of hydrogen evolution rates measured under identical experimental conditions. The main role of a co-catalyst in photocatalytic water splitting is to extract the photoexcited electrons from the CB while providing active sites for the gas evolution. Pure ethanol, employed as a sacrificial agent (hole scavenger) to suppress electron–hole recombination, yielded only 0.5 μmol h^{-1} of H_2 after 0.5 h of light irradiation (SI, Fig. S3), which corresponds to *ca.* 1/13 of the activity of Sr_2TiO_4, *ca.* 1/110 of $Sr_2TiO_3F_2$, *ca.* 1/160 of $Sr_3Ti_2O_7$, and *ca.* 1/5 of $Sr_3Ti_2O_5F_4$, underscoring that the observed H_2 evolution arises predominantly from the photocatalytic reaction rather than from decomposition of the sacrificial agent.

Apparent quantum yield (AQY) values are not reported because the immersion-type Hg lamp used provides multiple discrete emission lines that cannot be isolated to a single excitation wavelength, such that a single-wavelength AQY is not physically well defined; photocatalytic trends are therefore discussed based on hydrogen evolution rates measured under strictly identical conditions.

3 Computational methods

3.1 DFT band structure

To analyze the electronic structures of Sr_2TiO_4, $Sr_2TiO_3F_2$, $Sr_3Ti_2O_7$, and $Sr_3Ti_2O_5F_4$, we conducted density functional theory (DFT) calculations using the CASTEP package.[69] The plane-wave pseudopotential method with ultrasoft pseudopotentials was adopted to describe the electron–ion interactions, and the exchange–correlation energy was treated within the generalized gradient approximation (GGA) using the Perdew–Burke–Ernzerhof (PBE) function.[70] The plane-wave cut-off energy was set to 600 eV. Sr(4s, 4p, 5s), Ti(3s, 3p, 3d, 4s), O(2s, 2p), and F(2s, 2p) orbitals were treated as valence states. For each composition (on Sr_2TiO_4, $Sr_2TiO_3F_2$, $Sr_3Ti_2O_7$, and $Sr_3Ti_2O_5F_4$), the experimentally determined structures (space groups and atom types as refined from PXRD) were used as starting models, and only the atomic positions were relaxed using the Broyden–Fletcher–Goldfarb–Shannon (BFGS) algorithm prior to the electronic-structure analysis, in order to allow a reasonable comparison with the experimental data. Brillouin-zone integrations used Monkhorst–Pack[71] k-point mesh ($8 \times 8 \times 4$), dense enough to converge total energies and band dispersions. Band structures were computed along conventional high-symmetry paths, and partial densities of states (PDOSs) were obtained using atomic-orbital projections.

Hybrid-functional calculations using the screened Heyd–Scuseria–Ernzerhof (HSE06)[72,73] functional were carried out for Sr_2TiO_4 and $Sr_2TiO_3F_2$ within CASTEP. All computational parameters were identical to those used for the PBE calculations. A Monkhorst–Pack k-point mesh of $4 \times 4 \times 2$ was employed. Owing to the increased computational expense, HSE06 calculations were limited to $n = 1$ RP phases and used solely to assess the robustness of PBE-derived bandgap trends.

3.2 Effective mass evaluation

Electron effective masses[74] near the conduction-band minimum (CBM) were extracted by fitting the DFT band dispersion $E(k)$ in a small neighborhood of the CBM wavevector k_0. The effective-mass tensor m^*_{ij} is defined as:

$$\frac{m^*_{ij}}{m_0} = \frac{\hbar^2}{m_0}\left[\frac{\partial^2 E}{\partial k_i\,\partial k_j}\right]^{-1}_{k=k_0} \tag{11}$$

where m_0 is the free electron mass, $\hbar$ is the reduced Planck constant, and k is the reciprocal lattice vector. For the layered RP lattices, we report directional masses along the principal transport axes as follows:

$$m^*_{\parallel} = \frac{\hbar^2}{\left|\dfrac{\partial^2 E}{\partial k^2_{\parallel}}\right|_{k_0}} (\text{in-plane, curvature along } \Gamma \rightarrow X) \tag{12}$$

$$m^*_{\perp} = \frac{\hbar^2}{\left|\dfrac{\partial^2 E}{\partial k^2{}_{\perp}}\right|_{k_0}} (\text{out-of-plane, curvature along } \Gamma \rightarrow Z) \tag{13}$$

Second derivatives were evaluated from a symmetric finite-difference fit to $E(k)$ on a dense local k-mesh around k_0 (within a small window of $|k| = 0.01$ Å^{-1}).[75]

4 Results and discussion

4.1 Structure and phase analysis

Phase-pure RP-type oxides Sr_2TiO_4 ($n = 1$) and $Sr_3Ti_2O_7$ ($n = 2$) were synthesized *via* conventional solid-state methods and subsequently subjected to non-oxidative topochemical fluorination using PVDF, yielding the corresponding oxyfluorides $Sr_2TiO_3F_2$ and $Sr_3Ti_2O_5F_4$, in agreement with previously reported findings (Fig. 1).[51–54] For $n = 1$, Rietveld analysis confirmed that Sr_2TiO_4 ($I4/mmm$) transforms to $Sr_2TiO_3F_2$ with lower-symmetry tetragonal $P4/nmm$, consistent with the report by Slater and Gover,[53] and accompanied by a pronounced c-axis expansion upon fluoride anion (F^-) insertion (Fig. 2). Fluorination to $Sr_2TiO_3F_2$ substitutes apical oxide anions (O^{2-}) with

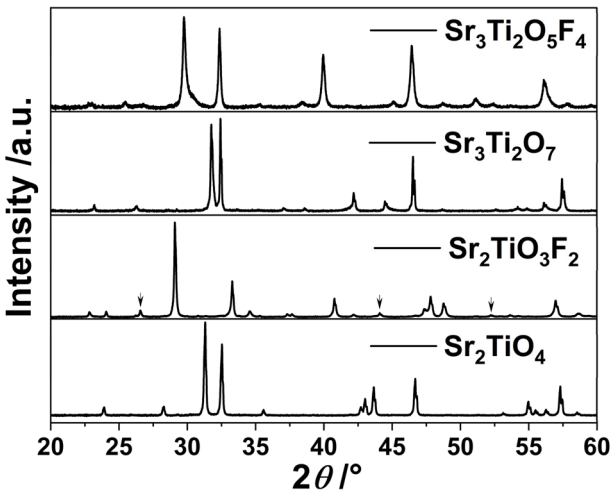

Fig. 1 XRD patterns of the synthesized compounds Sr_2TiO_4, $Sr_3Ti_2O_7$, $Sr_2TiO_3F_2$, and $Sr_3Ti_2O_5F_4$. The small arrows in the $n = 1$ phase for oxyfluoride, $Sr_2TiO_3F_2$, indicate the additional trace amount of SrF_2.

F^- and adds the second F^- to every second interstitial layer, altering the local Ti coordination to non-centrosymmetric TiO_5F units. This substitution breaks local inversion symmetry, resulting in an asymmetric anion distribution along the *c*-axis and inducing local polar distortions within the layered framework. A minor SrF_2 impurity (~3 wt%) was detected in the $n = 1$ fluorinated sample, consistent with the known metastability of $Sr_2TiO_3F_2$.[51,53] In contrast, the $n = 2$ phase, $Sr_3Ti_2O_7$, retains the tetragonal *I*4/*mmm* symmetry upon fluorination to $Sr_3Ti_2O_5F_4$, with lattice expansion along the *c*-axis in agreement with previous reports and in agreement with the fact that all interstitial sites must be filled in addition to the anion substitution with high interstitial layer filling.[52,76,77] This interpretation is further supported by the refined lattice parameters obtained by XRD in the present work, which are in close agreement with literature values reported by Wissel *et al.*,[51,52] from combined PXRD/neutron diffraction (ND) studies presented in Fig. 3. As ND provides higher precision for bond distances, particularly when light elements such as O^{2-} and F^- are involved, the results are used for a detailed discussion of local coordination. Our own PXRD-refined bond distances are nevertheless presented in Fig. 4 and Table 1 for completeness and direct comparison with ND taken from the literature.[51,52] The crystal structures obtained from Rietveld-refined XRD results are presented in Fig. 5. The lattice parameters from the present work, together with literature values for reference,[51,52] are provided in SI Tables S1 and S2. The structural models highlight differences in the local coordination environment for different *n* layers, as well as upon fluorination. For instance, Sr_2TiO_4 exhibits regular TiO_6 octahedral units, whereas

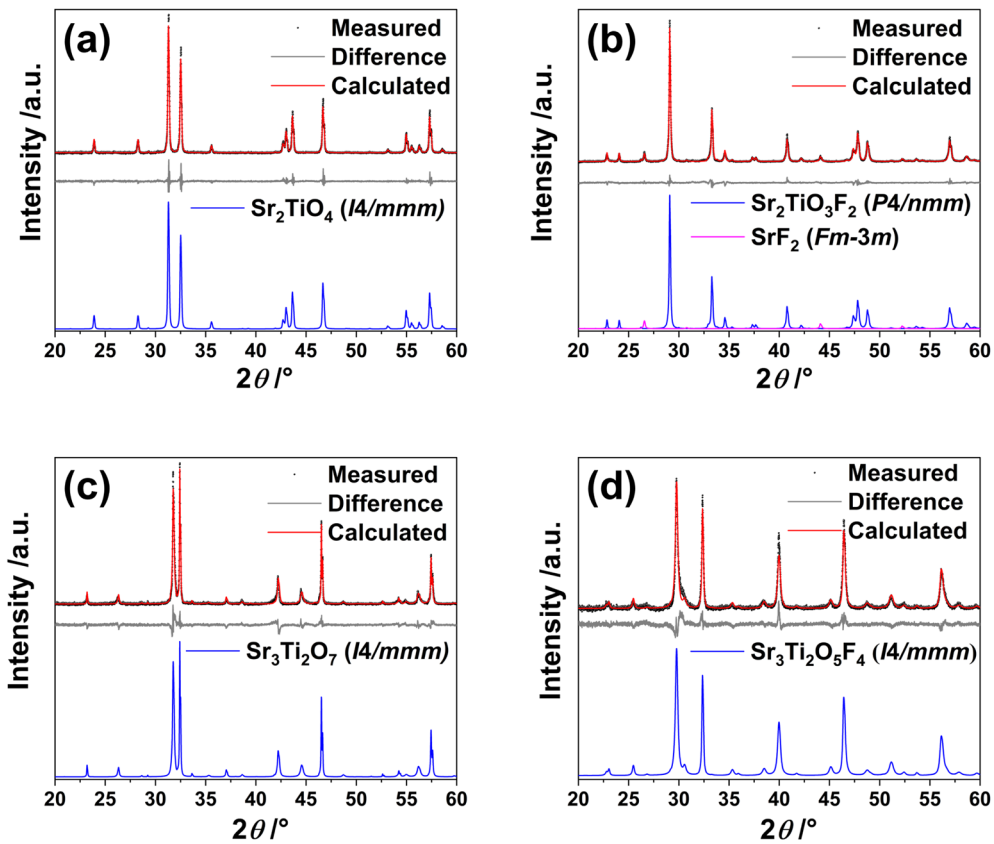

Fig. 2 Rietveld refinements of PXRD data: (a) Sr_2TiO_4, (b) $Sr_2TiO_3F_2$, (c) $Sr_3Ti_2O_7$, and (d) $Sr_3Ti_2O_5F_4$. The corresponding simulated reference patterns displayed in the lower part of each panel were generated and refined from ICSD/database structural models as described in Section 2.2.1. The Rietveld refinement quality indicators of the crystallographic analysis are provided in SI, Table S3.

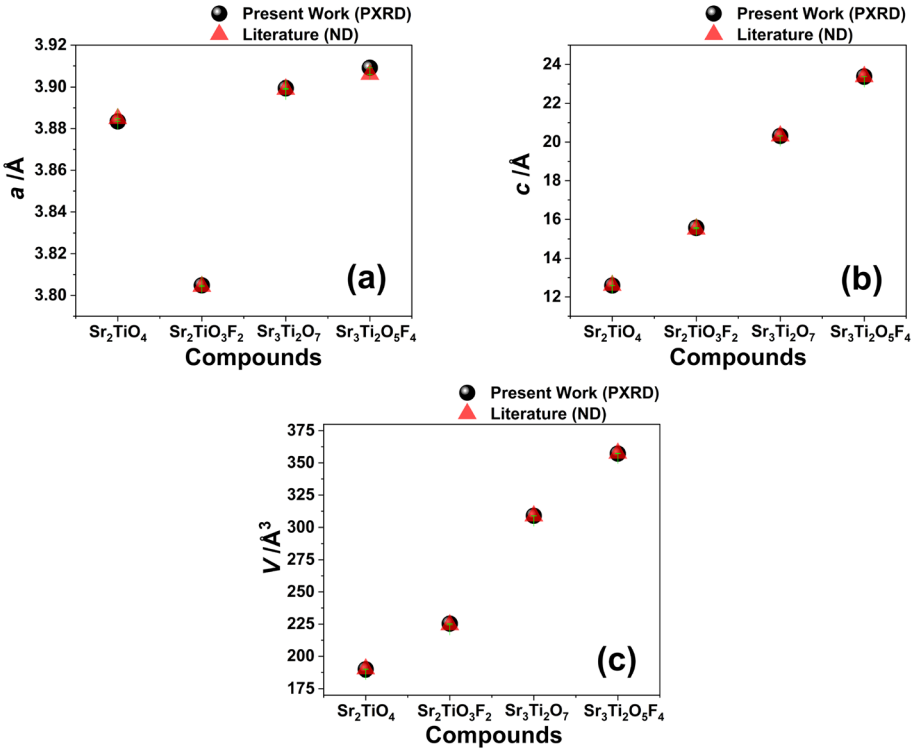

Fig. 3 Comparison of lattice parameters (a) *a*, (b) *c*, and (c) unit cell volume (*V*) obtained from Rietveld refinements (PXRD) of the present work (black circles) with reported literature values[51,52] (red triangles) from ND for Sr_2TiO_4, $Sr_3Ti_2O_7$, $Sr_2TiO_3F_2$, and $Sr_3Ti_2O_5F_4$.

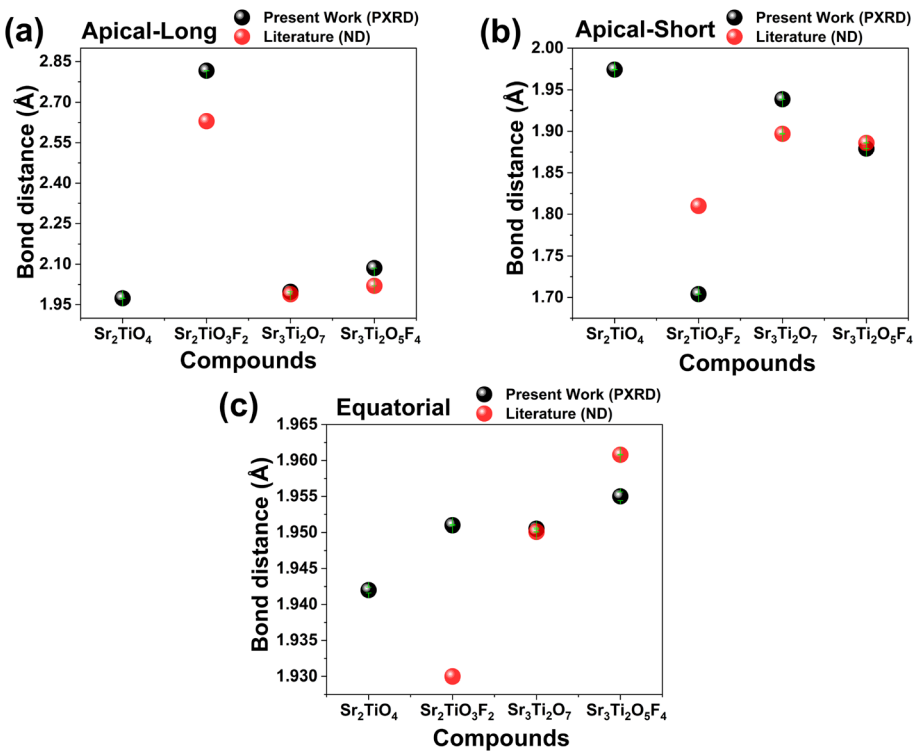

Fig. 4 Comparison of Ti–X (X = O, F) bond distances for Sr_2TiO_4, $Sr_3Ti_2O_7$, $Sr_2TiO_3F_2$, and $Sr_3Ti_2O_5F_4$: (a) apical-long, (b) apical-short, and (c) equatorial. The values obtained from Rietveld refinements (PXRD) of the present work (black circles) with reported literature values[51,52] (red circles) from ND. (see SI Tables S4 and S5).

Table 1 Summary of Ti–(O, F) coordination environments obtained from Rietveld refinements of Sr_2TiO_4, $Sr_2TiO_3F_2$, $Sr_3Ti_2O_7$, and $Sr_3Ti_2O_5F_4$ from PXRD, along with literature values from combined PXRD/ND[51,52] for comparison

		Ti–O coordination		Ti–(O, F) coordination			
		Equatorial Ti–O (Å)		Apical short (Å)		Apical long (Å)	
Phase	Ti-coordination environment	Present work	Literature	Present work	Literature	Present work	Literature
Sr_2TiO_4	TiO_6 (regular)	1.942(4)	—	1.974(3)	—	1.97(4)	—
$Sr_2TiO_3F_2$	TiO_5F/TiO_4F_2 (locally asymmetric)	1.951(1)	1.93	1.701(4)	1.81	2.81(6)	2.63
$Sr_3Ti_2O_7$	TiO_6 (regular, locally polar)	1.950(2)	1.9501(1)	1.742(8)	1.989(2)	1.97(3)	1.897(5)
$Sr_3Ti_2O_5F_4$	TiO_6/TiO_5F (nearly regular)	1.96(5)	1.9608(4)	1.89(9)	1.886(2)	2.01(4)	2.020(3)

$Sr_2TiO_3F_2$ adopts a locally non-centrosymmetric TiO_5F coordination due to the breaking of inversion symmetry. Interestingly, even in the $n = 2$ oxide ($Sr_3Ti_2O_7$), a slight off-center displacement of Ti is observed, arising from octahedral tilting and the non-centrosymmetric site symmetry of Ti. These intrinsic deviations from ideal symmetry indicate that local polarity is already present in the oxide phase and correlate with the variations in bond distances shown in Table 1 and Fig. 4. As discussed later in Section 4.5, fluorination of $Sr_3Ti_2O_7$ to $Sr_3Ti_2O_5F_4$ removes this off-center distortion, suggesting that polarity effects are unlikely to contribute to the photocatalytic activity of the $n = 2$ RP-type phases.

PXRD measurements performed after soaking all four synthesized RP-type oxides and oxyfluorides in deionized water (DI-H_2O) for 24 h (Fig. S4) confirm that they retain their phase without signs of structural degradation, assuring that the photocatalytic trends discussed later (Section 4.5) originate from intrinsic structural and electronic properties rather than instability or hydration-induced transformations. In addition, PXRD data from aged samples for ~1.5 years stored under ambient conditions were also recorded to further assess their long-term stability, and the corresponding Rietveld analyses (Fig. S5) confirm that all phases remain stable, with only a trace amount of $SrCO_3$ (3.1(1) wt%) detected in the $n = 2$ oxide, $Sr_3Ti_2O_7$.

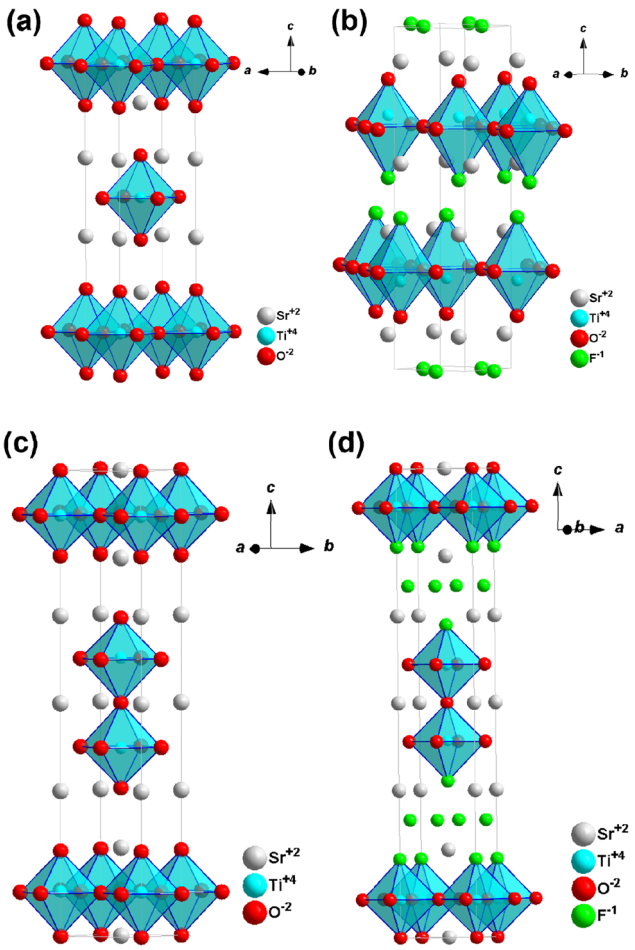

Fig. 5 Crystal structures obtained from refined XRD data before and after topochemical fluorination reactions: (a) Sr_2TiO_4, (b) $Sr_2TiO_3F_2$, (c) $Sr_3Ti_2O_7$, and (d) $Sr_3Ti_2O_5F_4$.

4.2 Optical properties and band-edge potential evaluation by the Butler–Ginley approach

The UV-Vis DRS and the corresponding Kubelka–Munk plots of the RP oxides with $n = 1$ and 2, and their fluorinated oxyfluoride compounds, are shown in Fig. 6 and S6. Both pristine Sr_2TiO_4, and $Sr_3Ti_2O_7$ display sharp absorption edges in the ultraviolet region (Fig. 6a and b; black lines), with very similar estimated band gap values of 3.52 eV and 3.44 eV, respectively (Fig. 6c and d; black lines), consistent with earlier reports for undoped RP-type titanates.[17–19,21–23] Upon topochemical fluorination for $n = 1$, $Sr_2TiO_3F_2$ exhibits two absorption onsets at 3.36 eV and 3.69 eV (Fig. 6a and c; red lines; and Fig. S6b), compared to 3.52 eV in Sr_2TiO_4, indicating that fluorination has only a very minor influence on the fundamental band gap, with the lower-energy onset corresponding to a small red shift of ~0.16 eV. In comparison, the higher onset reflects a slight blue shift of ~0.17 eV. This small change can be attributed to structural distortions in the TiO_6-octahedra upon fluorination, where incorporation of fluorine produces ordered, asymmetric TiO_5F coordination. Substitution of apical O^{2-} by F^- breaks inversion symmetry along the *c*-axis, inducing local dipole fields that can modify the electronic band structure. Such effects are well documented in other fluorinated RP-type phases[27,37,78] and are reflected here by the symmetry lowering from *I*4/*mmm* to *P*4/*nmm*, which generates inequivalent anion coordination environments that can modify the electronic band structure. DFT calculations by Wissel *et al.*[51] further support this interpretation, showing that ordered TiO_5F environments represent the most stable configuration in

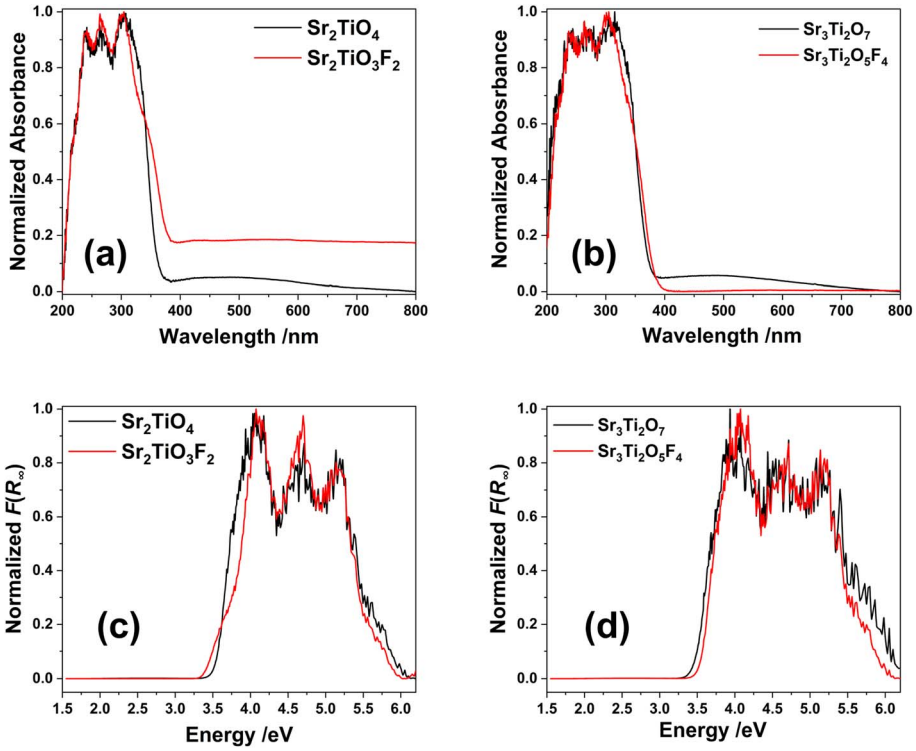

Fig. 6 UV-Vis DRS normalized absorbance spectra of oxides and oxyfluorides of $n = 1$ (a) and $n = 2$ (b), and their respective normalized Kubelka–Munk '$F(R_\infty)$' plots (c and d). The individual Kubelka–Munk plots with extracted energy slopes are provided for better clarity in the SI Fig. S6.

$Sr_2TiO_3F_2$, in line with our experimental observations. Similar symmetry-lowering and polarisation effects have been reported for fluorine-expedited nitridation of layered perovskite Sr_2TiO_4 to Sr_2TiO_3NF, where the altered octahedral geometry shifts the conduction band minimum (CBM) through modified Ti 3d-(O, F) 2p orbital overlap.[20]

The optical changes are less pronounced for the $n = 2$ phase, $Sr_3Ti_2O_5F_4$ (Fig. 6b and d, red lines), which shows a slight blue-shift of ~0.07 eV in the absorption edge relative to the parent oxide $Sr_3Ti_2O_7$, which is well within the typical DRS uncertainty for bandgap estimates. This modest increase is consistent with the greater structural rigidity of the double-layer RP framework, which can better accommodate apical O^{2-} to F^- substitution without large distortions. In addition, the higher electronegativity of F^- likely contributes to stabilizing the valence band maximum (VBM) through stronger localization of O/F 2p states, thereby shifting the absorption onset to higher energies. Similar band-structure adjustments driven by local electrostatic effects have been outlined by Kato *et al.* for layered oxyhalide and oxyfluoride systems, even when the bulk bandgap remains nearly unchanged.[37,79] In our case, the Kubelka–Munk plots (Fig. 6d and S6c, d) show clean absorption edges for both oxides and oxyfluorides, without significant sub-gap features. The absorption features observed in the 200–350 nm region correspond to intrinsic interband electronic transitions, dominated by charge-transfer excitation from O 2p derived valence band states to Ti 3d derived conduction band states, which are characteristic of Sr–Ti–O-based wide-bandgap oxides. These higher-energy UV transitions reflect the fundamental titanate electronic framework.[80] This indicates that fluorination does not introduce optically active deep defect states, and the fundamental absorption edge remains well preserved. Such behavior aligns with previous reports on fluorinated RP materials, where controlled anion substitution adjusts band structure while maintaining favorable charge-carrier dynamics.[78] Overall, the fluorination-induced changes in Sr_2TiO_4 and $Sr_3Ti_2O_7$ reflect trends reported in related mixed-anion layered perovskites, with modest bandgap shifts, local polar distortion through symmetry breaking, and the maintenance of an electronically clean gap.

Experimentally, the $n = 2$ phase ($Sr_3Ti_2O_7$/$Sr_3Ti_2O_5F_4$) shows a wider band gap compared to the $n = 1$ phase (Sr_2TiO_4/$Sr_2TiO_3F_2$), as seen from the absorption edge positions in Fig. 6. This widening reflects the role of increased perovskite layer thickness in RP structures, where the double-layered framework reduces structural distortions and modifies orbital interactions, leading to a higher optical band gap. This is interesting, since in perovskites (oxynitrides), a reduction of structural distortion leads to a smaller band gap because the B–X orbital overlap becomes stronger as the B–X–B angle approaches 180°.[81,82] However, in the oxyfluoride RP system here, this narrowing tendency is offset by oxide to fluoride substitution, which reduces p–d covalency and lowers the VBM. Consequently, the narrower band gap in the $n = 1$ phase enables stronger absorption in the near-UV region, which is expected to contribute more effectively to photocatalytic H_2 evolution under solar irradiation. These modifications are expected to contribute to the enhanced photocatalytic H_2 evolution observed for the $n = 1$ oxyfluoride, as will be discussed in Section 4.5.

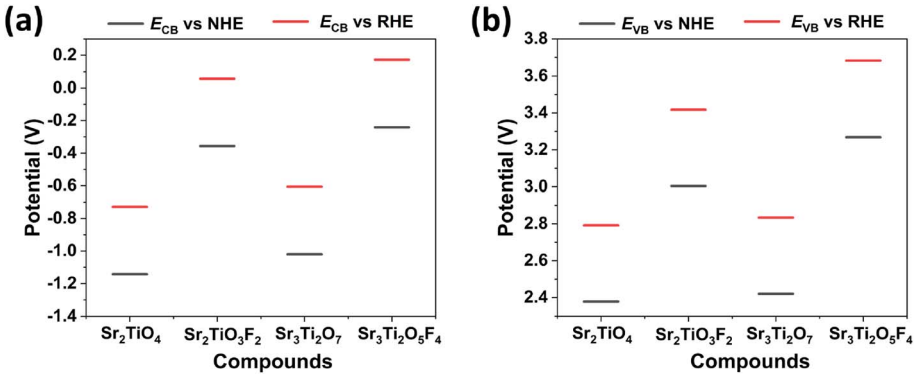

Fig. 7 Band-edge positions for the oxides and oxyfluorides of $n = 1$ (a) and $n = 2$ estimated by the Butler–Ginley method by using UV-Vis-DRS energy bandgap values. (a) Conduction band edge E_{CB}; (b) valence band edge E_{VB}. Black and red markers show values *vs.* NHE and RHE, respectively, at pH 7.

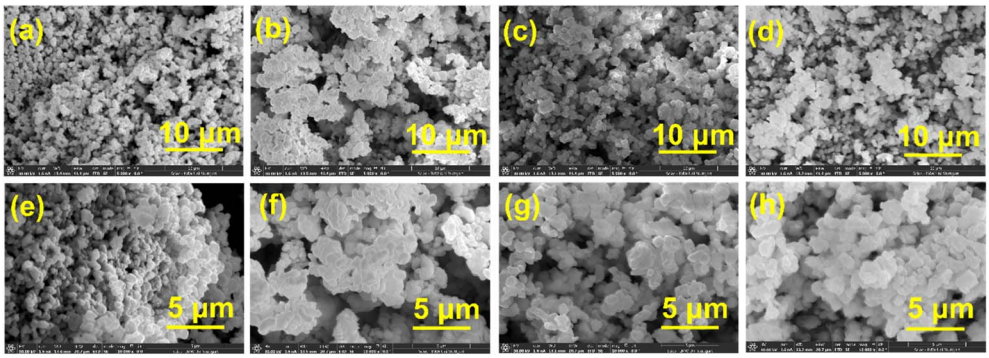

Fig. 8 SEM images displayed in the upper panels (a–d) correspond to Sr_2TiO_4, $Sr_3Ti_2O_7$, $Sr_2TiO_3F_2$, and $Sr_3Ti_2O_5F_4$ samples, recorded at a scale of 10 μm. The lower panels (e–h) show the corresponding higher-magnification images of the same samples (a–d), respectively, recorded at a scale of 5 μm.

4.2.1 Band-edge alignment from UV-Vis-DRS + Butler–Ginley. Using the bandgap energies from UV-Vis DRS results and a consistent Mulliken electronegativity set,[59–65] we estimated the conduction- and valence-band edges (E_{CB} and E_{VB}) *vs.* NHE, presented in Fig. 7 (also in SI, Tables S6 and S7). The topochemical fluorination shifts both band edges to more positive potentials. For $n = 1$, the conduction band changes from −1.1(2) V for Sr_2TiO_4 to −0.4(2) V for $Sr_2TiO_3F_2$, while the valence band changes from +2.4(2) V to +3.0(2) V. For $n = 2$, the conduction band changes from −1.0(2) V for $Sr_3Ti_2O_7$ to −0.2(2) V for $Sr_3Ti_2O_5F_4$, and the valence band changes from +2.4(2) V to +3.3(2) V. These shifts reduce the conduction-band driving force for H^+/H_2 in both series ($\Delta E_{CB} \approx +0.8 \pm 0.3$ V), while the valence band deepens by ∼0.6–0.9 ± 0.3 V, reproducing the small experimental changes in E_g. On an RHE basis at pH 7.0, $Sr_3Ti_2O_5F_4$ has the least favorable CB position (+0.2(2) V *vs.* RHE), consistent with its low photocatalytic H_2 evolution activity, whereas $Sr_2TiO_3F_2$ lies very close to the H^+/H_2 level (+0.06(20) V *vs.* RHE) and, aided by inversion-symmetry breaking in TiO_5F units and the resulting internal dipoles, exhibits enhanced H_2 evolution (Section 4.5).

It should be noted that experimental determination of band-edge positions by Mott–Schottky analysis or valence-band XPS is feasible for photocatalytic systems that can be fabricated as stable, electronically conductive electrodes or heterojunctions.[83,84] In contrast, the RP-type titanate oxide and oxyfluoride phases studied here, are highly insulating, micron-scale powders, for which such measurements are not reliable without altering the material chemistry. Under these constraints, the Butler–Ginley approach provides an appropriate framework for comparing relative band-edge trends based on experimentally determined optical band gaps, although absolute energetic alignment is not implied.

4.3 Morphological properties and BET surface area analysis

The SEM micrographs in Fig. 8 show the morphologies of Sr_2TiO_4, $Sr_3Ti_2O_7$, and their oxyfluoride phases $Sr_2TiO_3F_2$ and $Sr_3Ti_2O_5F_4$. All compounds consist of irregular, rounded grains in the submicrometer to micrometer range, typical of solid-state synthesized RP-type titanates. The particles form loosely packed agglomerates with clean surfaces and without indications of secondary phases. The topochemical fluorination, carried out at low temperatures using PVDF, does not induce noticeable morphological changes in either $n = 1$ or 2 systems. The fluorinated products maintain the overall particle size distribution and shape of their oxide precursors, indicating that the process

preserves the bulk morphology while modifying only the anion sublattice at the atomic scale, as expected for a topochemical reaction.[34] Again, this morphological stability is critical for interpreting the photocatalytic results, as it ensures that the observed differences in H_2 evolution activity arise from intrinsic structural and electronic effects rather than changes in particle size or morphologies.

The N_2 adsorption–desorption isotherms of Sr_2TiO_4, $Sr_2TiO_3F_2$, $Sr_3Ti_2O_7$, and $Sr_3Ti_2O_5F_4$ (SI Fig. S7) display low overall uptake, consistent with non-porous or only weakly porous solids composed of aggregated particles, as also observed in the SEM images (Fig. 8). Minor hysteresis features appear at higher relative pressures, which may be attributed to interparticle voids.[85] The measured BET surface areas are 7.71 $m^2\ g^{-1}$, 5.67 $m^2\ g^{-1}$, 2.78 $m^2\ g^{-1}$, and 3.91 $m^2\ g^{-1}$ for Sr_2TiO_4, $Sr_2TiO_3F_2$, $Sr_3Ti_2O_7$, and $Sr_3Ti_2O_5F_4$, respectively. These values are typical of dense, solid-state-synthesized RP-type titanates and show no significant variation upon fluorination. The low surface areas of the powders, with only small differences between samples (<10 $m^2\ g^{-1}$), are therefore not interpreted as the primary factor governing the photocatalytic trends between the $n = 1$ and $n = 2$ members.

4.4 XPS analysis

XPS was performed to investigate the oxidation states and chemical environments of the $n = 1$ and 2 oxides and their oxyfluorides. These results were further correlated with the structural features obtained from PXRD and compared with the spectra of the parent oxides, as shown in Fig. 9. All binding energies were referenced to the adventitious C 1s peak at 285 eV (SI Fig. S8a).

The Ti 2p spectra (Fig. 9a) of all compounds show the characteristic doublet, with Ti $2p_{3/2}$ at ~458.5 eV and $2p_{1/2}$ at ~464.1 eV (spin–orbit splitting (Δ) ≈ 5.7 eV). Across both $n = 1$ and 2 samples, these binding energies vary by no more than 0.2–0.4 eV, consistent with Ti^{4+} in octahedral coordination within the perovskite slabs.[51,52,86] In compared to the other samples, which show symmetric Ti 2p peaks in the XPS spectrum (Fig. S9), a small shoulder to lower binding energies can be observed for $Sr_3Ti_2O_5F_4$. This indicates that a slightly non-homogeneous O/F distribution around the Ti ions might be present; alternatively, a small Ti^{3+} contribution might explain this observation. However, since $Sr_3Ti_2O_5F_4$ exhibits a positive-chemical shift of about +0.4 eV relative to Sr_2TiO_4, $Sr_2TiO_3F_2$, and $Sr_3Ti_2O_7$, and the compound is entirely white in visual inspection, this makes the structural O/F defects more likely than a Ti^{3+} contribution.

Structural refinements from XRD (Fig. 2 and5) support this interpretation. In the parent $n = 2$ oxide $Sr_3Ti_2O_7$, TiO_6 octahedra are locally distorted, with one shorter apical Ti–O bond (1.74–1.90 Å) and a longer apical contact (~1.99 Å), reflecting a slight off-centre displacement of Ti within the octahedron. Upon fluorination, the $n = 2$ oxyfluoride $Sr_3Ti_2O_5F_4$ adopts a more centrosymmetric coordination environment, with an equatorial Ti–(O/F) distance of ~1.96 Å and nearly balanced

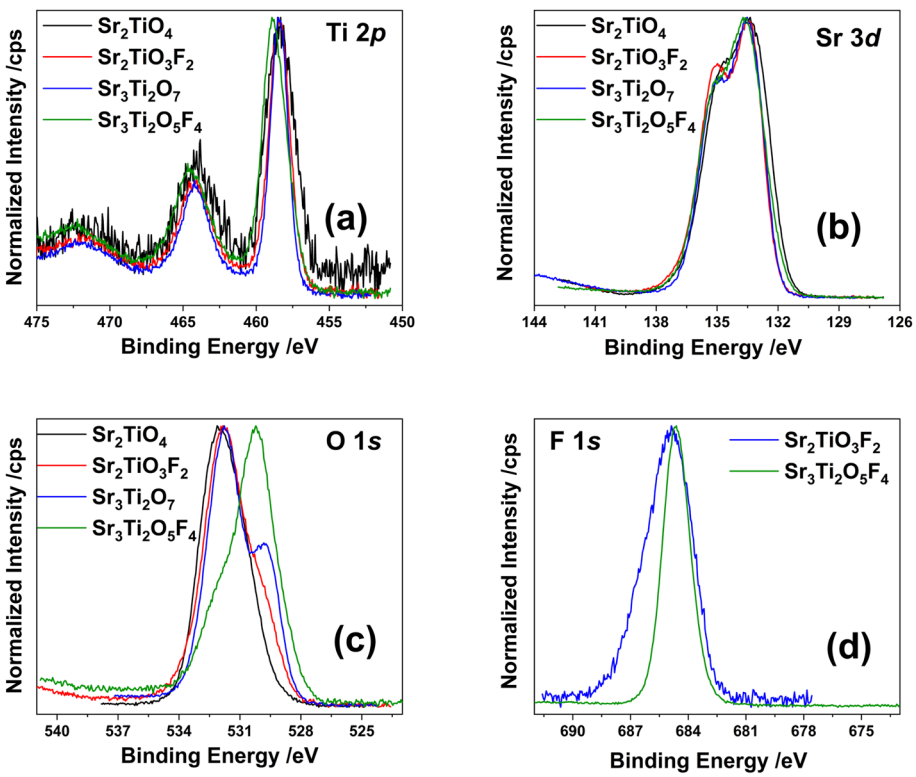

Fig. 9 XPS spectra of Sr_2TiO_4, $Sr_2TiO_3F_2$, $Sr_3Ti_2O_7$, and $Sr_3Ti_2O_5F_4$ showing the Ti 2p (a), Sr 3d (b), O 1s (c), and F 1s (d) regions. The C 1s calibration peak and an enlarged Ti 2p region highlighting the chemical shift in $Sr_3Ti_2O_5F_4$ are provided in SI Fig. S8a and b and S9, respectively.

apical bonds of ~1.89/2.02 Å. This restoration of local symmetry enhances the average Ti–(O, F) interaction and increases the electrostatic potential at the Ti site, explaining the observed +0.45 eV upshift. By contrast, the $n = 1$ oxyfluoride, $Sr_2TiO_3F_2$, exhibits a pronounced off-centre displacement with a very short Ti–O bond (~1.70–1.81 Å) and a very long Ti–F bond (~2.63–2.81 Å), thereby the coordination becomes highly asymmetric locally. This asymmetric environment creates strong local dipoles and increased Ti–O covalency (slightly more ionic Ti–F *vs.* Ti–O), which stabilizes the Ti states and prevents a comparable shift in binding energy. Overall, the XPS results indicate that Ti remains essentially in the Ti^{4+} state across both $n = 1$ and $n = 2$ systems.

The Sr 3d spectra (Fig. 9b) exhibit the characteristic Sr^{2+} doublet, with $3d_{5/2}$ at ~132.9–133.5 eV and $3d_{3/2}$ at ~135.2 eV ($\Delta \approx$ 1.8 eV),[87] confirming that Sr remains divalent upon fluorination. The binding energies are essentially unchanged between the $n = 1$ (Sr_2TiO_4/$Sr_2TiO_3F_2$) and $n = 2$ ($Sr_3Ti_2O_7$/$Sr_3Ti_2O_5F_4$) samples. Structural refinements suggest that this arises from fluorine incorporation at the interlayer X4 sites (Sr_2–F ≈ 2.47 Å) and shortened Sr–X3 distances, which generate in a more symmetric Sr coordination environment. This stabilization reduces the reactivity of the rock-salt layers toward carbonate formation upon exposure to air, consistent with the reduced O 1s shoulder at ~531–532 eV (Fig. 9c). Importantly, this surface feature is limited to adsorbates and does not indicate a change in the bulk Sr oxidation state.

The O 1s (Fig. 9c) core level is dominated by the lattice O^{2-} at ~529.0–530.5 eV of Ti oxide and 531.5 eV of Sr oxide, with a minor shoulder at ~532.0–532.5 eV assigned to surface carbonates.[87,88] The $n = 2$ RP structure exhibits a higher degree of built-in structural anisotropy than the $n = 1$ phase due to the presence of distinct perovskite slab and rock-salt layers, which gives rise to multiple nonequivalent anion environments.[11–16] Notably, the intensity of this carbonate feature is weakest for $Sr_3Ti_2O_5F_4$, consistent with its reduced tendency for surface carbonate formation. In addition, the lattice O contribution in $Sr_3Ti_2O_5F_4$ appears slightly shifted to higher binding energy. This observation matches the XRD results, where fluorination produces nearly balanced (relatively less asymmetric to $n = 2$ oxide) apical Ti–(O, F) distances and a more symmetric octahedral field, which reduces Ti–O covalency and increases the average electrostatic potential on oxygen. In contrast, $Sr_2TiO_3F_2$ retains highly asymmetric Ti–O and Ti–F distances, which enhance Ti–O hybridization and stabilize O at a lower binding energy.[51,52]

The F 1s spectra (Fig. 9d) for the oxyfluoride samples $Sr_2TiO_3F_2$ and $Sr_3Ti_2O_5F_4$ confirm the incorporation of fluorine into the lattice and exhibit a single symmetric F 1s characteristic peak at ~684.5 ± 0.2 eV. Likewise, the peak in $Sr_3Ti_2O_5F_4$ is narrower and shifted slightly to lower binding energy compared with $Sr_2TiO_3F_2$, which reflects the more regular fluorine incorporation in the $n = 2$ oxyfluoride. XRD analysis supports this interpretation, showing that in $Sr_3Ti_2O_5F_4$ fluorine preferentially occupies the interlayer X4 and apical-terminal X3 positions with well-defined Sr–F and Ti–F bond lengths, whereas in $Sr_2TiO_3F_2$ fluorine resides in a strongly asymmetric environment that broadens the F 1s signal.

Overall, the XPS results confirm the presence of Ti^{4+} and Sr^{2+} in all samples, highlighting a structural influence on the observed chemical shifts. This structural difference explains the unique 0.4 eV shift visible in the Ti 2p core level for the sample $Sr_3Ti_2O_5F_4$ compared with Sr_3TiO_4 and its reduced tendency toward carbonate formation compared with the parent oxide.

4.5 Photocatalytic hydrogen evolution performance

Photocatalytic H_2 evolution experiments were performed for the RP-type oxides and their oxyfluorides and are shown in Fig. 10. For $n = 1$, fluorination of Sr_2TiO_4 to $Sr_2TiO_3F_2$ yields an exceptional enhancement in photocatalytic activity, with an initial H_2 evolution rate ~6.3-fold higher than the parent oxide, Sr_2TiO_4, and still ~5-fold higher after 2 h of continuous light irradiation. In contrast, for $n = 2$, the oxide $Sr_3Ti_2O_7$ exhibits significantly higher activity (~30-fold) than its oxyfluoride $Sr_3Ti_2O_5F_4$ and remains ~26-fold after 2 h of light irradiation. As summarized in Fig. 10c, both oxyfluorides show a decline in activity relative to their initial rates after 2 h irradiation. $Sr_2TiO_3F_2$ ($n = 1$) still retains ~5-fold the activity of Sr_2TiO_4, suggesting that local polarity-induced internal fields enhance charge separation and help sustain photocatalytic activity over time, while the

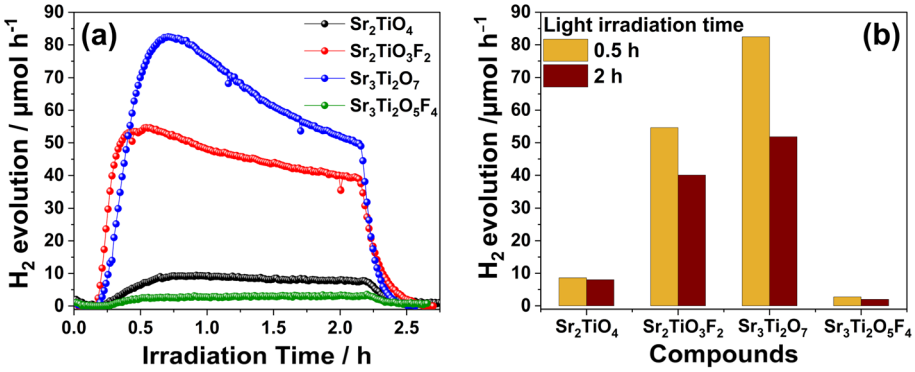

Fig. 10 Photocatalytic H_2 evolution activity of RP oxides and their respective oxyfluorides: (a) Sr_2TiO_4, $Sr_2TiO_3F_2$, $Sr_3Ti_2O_7$, and $Sr_3Ti_2O_5F_4$. (b) Comparison of H_2 evolution amounts for each compound at 0.5 h and 2 h of light irradiation. Reproducibility of the photocatalytic H_2 evolution and the phase stability after photocatalytic performance for the most active sample, $Sr_3Ti_2O_7$, are provided in the SI, Fig. S10, S11 and Table S8.

structural stability is primarily ensured by the RP framework itself. In contrast, the activity of $Sr_3Ti_2O_5F_4$ ($n = 2$) decays almost completely, which could be related to the formation of charge recombination centers as suggested for similar anion-substituted titanates in the literature.[37,78,79] However, further study is required to confirm the exact mechanism in this system. XPS analysis (Section 4.4 and Fig. 9) revealed a slight low-binding-energy shoulder in $Sr_3Ti_2O_5F_4$, suggesting minor local variations in the Ti–(O, F) coordination environment that could give rise to localized states within the band gap. Such structural or electronic inhomogeneities can promote carrier trapping and non-radiative recombination, thereby explaining the markedly low H_2 evolution activity of $Sr_3Ti_2O_5F_4$.[89–92]

For $n = 1$, $Sr_2TiO_3F_2$ (Fig. 10a), the higher activity can be rationalized from the structural point of view, as discussed in Section 4.1, as well as using the refined bond distances from the reported neutron diffraction,[51,52] which provide the most precise bond distances for O/F coordination. The refined bond distances provide crucial insight into how topochemical fluorination modifies the local Ti coordination and thereby impacts photocatalytic performance (Fig. 4, 5, Tables 1, SI S4 and S5). In $n = 1$, Sr_2TiO_4, the TiO_6 octahedra are centrosymmetric, with an equatorial Ti–O bond length of ≈1.93 Å and an apical bond length of ≈1.97 Å. Upon fluorination to $Sr_2TiO_3F_2$, however, a pronounced distortion is introduced with one very short Ti–F/O bond of ∼1.81 Å and a long, weak apical bond of ∼2.63 Å, together with equatorial Ti–O ≈1.93 Å. This distortion effectively transforms the octahedral environment into a square-pyramidal-like TiO_5F unit, comprising four equatorial oxygen atoms, one short apical bond, and one very weak apical interaction, breaking inversion symmetry at the local Ti site, even though the global structure remains *P4/nmm* (centrosymmetric). Such asymmetric coordination is characteristic of second-order Jahn–Teller (SOJT) distortions, where hybridization between Ti 3d and O/F 2p orbitals stabilizes an off-center displacement of Ti within the octahedron.[93] The resulting lattice polarization generates internal dipole fields oriented along the *c*-axis, and in accordance with previous findings, such polar environments around Ti cations, whose states dominate the CB, facilitate charge separation and suppress electron–hole recombination, which can account for the enhanced H_2 evolution observed for $Sr_2TiO_3F_2$ relative to the parent oxide, Sr_2TiO_4. Yu and Xu reported that topochemical fluorination of Cr-doped Sr_2TiO_4 yields $Sr_2Ti_{0.95}Cr_{0.05}O_3F_2$ with an uneven O/F distribution that creates a built-in electric field, improves charge separation, and resulted in efficient H_2 evolution.[49]

By contrast, in $n = 2$, $Sr_3Ti_2O_7$ already shows locally non-centrosymmetric TiO_6 units, with the following bond lengths extracted by using neutron diffraction:[52] an equatorial Ti–O bond length of ≈1.95 Å and apical bond lengths of ≈1.90 Å (short) and 1.99 Å (long), consistent with the local site symmetry of *4mm* in this structure type (Fig. 5c). Upon fluorination to $Sr_3Ti_2O_5F_4$, the apical asymmetry reduces and the apical distances converge to ≈1.89 Å (short) and ≈2.02 Å (long), *i.e.*, become more similar, while the equatorial bond remains nearly unchanged (≈1.96 Å) (Fig. 5d and Table 1). As a result, the coordination $TiO_{6-x}F_x$ units generate a lower internal field due to the lower difference of apical bond lengths. This lower local polarity may account for the suppressed photocatalytic activity of $Sr_3Ti_2O_5F_4$ relative to the parent oxide $Sr_3Ti_2O_7$ shown in Fig. 10b. Furthermore, defect states introduced by the disorder might dominate the photocatalytic behavior of the material and could act as charge-carrier traps and recombination sites, thereby suppressing photocatalytic activity.[20,94–97]

Among the studied compounds, $Sr_3Ti_2O_7$ ($n = 2$) exhibits the highest photocatalytic activity (Fig. 10b). This trend is consistent with earlier reports,[11] which emphasize that the photocatalytic performance of RP perovskites is strongly dependent on the number of perovskite layers (n). A higher n facilitates more efficient spatial separation of photogenerated electrons and holes, thereby suppressing charge recombination.[37,98] Xiao *et al.* showed that higher homologues of RP-type members benefit from enhanced three-dimensional connectivity and improved bulk carrier mobility, leading to more favorable charge transport and band-edge alignment. This aligns with our present study, where the $n = 2$ phase $Sr_3Ti_2O_7$ demonstrates superior H_2 evolution activity compared to its $n = 1$ homologue.

In addition to symmetry effects, the feasibility of H_2 evolution also depends on the band alignment relative to the normal hydrogen electrode (NHE), which is numerically equivalent to the standard hydrogen electrode (SHE), at pH 0. According to literature reports, the CB edge of Sr_2TiO_4 is located nearly at −0.17 V *vs.* NHE/SHE, providing only a modest overpotential for H_2 generation.[18] This value is slightly more negative than the standard required H^+/H_2 potential, ensuring thermodynamic feasibility. For example, the layered Sillén oxyhalide, $SrBi_3O_4Cl_3$ and RP-type titanates exhibit CB levels sufficiently more negative than the proton reduction potential, supporting their intrinsic ability for proton reduction.[18,36] In this work, the electrochemical flat-band potentials were not determined (*e.g.*, by Mott–Schottky or UPS) for these RP-type titanates, instead we estimated band edges using the Butler–Ginley approach applied to the UV-Vis-DRS gaps, the resulting CB positions (*vs.* NHE) are −1.1(2) V (Sr_2TiO_4), −0.4(2) V ($Sr_2TiO_3F_2$), −1.0(2) V ($Sr_3Ti_2O_7$), and −0.2(2) V ($Sr_3Ti_2O_5F_4$), with corresponding VB positions of +2.4(2), +3.0(2), +2.4(2), and +3.3(2) V, respectively (Fig. 7). These Butler–Ginley estimates are consistent with previous reports on related oxyhalide and oxyfluoride systems, which indicate that their band edges fall within the suitable window for photocatalytic H_2 evolution.[18,36] For comparison with electrochemical data, NHE-referenced energies are converted to RHE (see Section 2.2.2.1, Tables S6 and S7). Since the Butler–Ginley approach is semi-empirical and flat-band potentials depend on surface/electrolyte conditions, we emphasize that our interpretation focuses on relative changes across the series rather than exact absolute numbers.

Within this framework, the reduced performance of $Sr_3Ti_2O_5F_4$ can be rationalized by the upward (less negative values) CB shift to −0.2(2) V *vs.* NHE (≈+0.2 (2) V *vs.* RHE at pH 7), in agreement with the slightly increased band gap, thereby reducing the thermodynamic driving force for proton (H^+) reduction in addition to the reduced local polar moment around Ti cations. By contrast, in $Sr_2TiO_3F_2$, the CB remains sufficiently negative *vs.* NHE (−0.4(2) V) and is counterbalanced by inversion-symmetry breaking and the

resulting internal dipole fields, which promote charge separation and surface reaction kinetics, explaining the pronounced enhancement in H_2 evolution. It is also interesting to see this relative trend in our previous findings in the RP-type indate system.[33] By using the published UV-Vis DRS energy gaps and Butler–Ginley estimates for the indates, as mentioned in Section 2.2.2.1, the band edge potentials were estimated and compared (Tables S6 and S7). As these studies used the same topochemical synthesis protocol and photocatalytic H_2 evolution conditions, the fluorination of RP-type $LaBaInO_4$ (*I*4/*mmm*) to $LaBaInO_3F_2$ (*C*2/*c*) preserves the conduction-band driving force, with E_{CB} of about −0.37 V *vs.* NHE for $LaBaInO_4$ and −0.41 V *vs.* NHE for $LaBaInO_3F_2$ (≈+0.05 V and 0.00 V *vs.* RHE at pH 7). Although the local coordination changes from centrosymmetric InO_6 octahedra to centrosymmetric InO_4F_2 and the E_{VB} deepens from +1.43 V to +2.89 V, thereby H_2 activity rates remain similar upon fluorination.[33] This highlights anion sublattice engineering as a selective strategy to tune symmetry and photocatalytic functionality in layered perovskite oxyfluorides. Future efforts should use alternative synthesis routes to tune the band gap toward the near-UV/visible and modestly increase accessible surface area. This suggests that beyond structural distortions, surface properties such as wettability and controlled morphological design will be critical for achieving stable and optimized performance in future oxyfluoride photocatalysts.[42,99,100] Effective synthesis should preserve a sufficiently negative E_{CB} so that, under illumination, the quasi-Fermi level for electrons remains above the H^+/H_2 level, while suppressing deep traps that hold the Fermi level and reduce beneficial band bending at the solid–liquid interface.

To assess the robustness of photocatalytic performance, reproducibility tests were carried out for the most active photocatalyst, $Sr_3Ti_2O_7$, and was characterized two more times in the already mentioned photocatalysis setup, using three independent photocatalytic runs performed under identical experimental conditions presented in SI, Fig. S10. All three independent measurements exhibit a rapid increase in H_2 evolution upon illumination, followed by a gradual decrease during the 2 h irradiation period and consistent behavior upon switching off the light. After 2 h, all runs converge to a H_2 evolution rate of approximately 50 μmol h^{-1}, confirming the reproducibility of the H_2 evolution reaction (HER) activity (Fig. S10). It's worth mentioning that the activity during the initial increase after turning the lamp on may vary from experiment to experiment. This is a known phenomenon observed at Pt co-catalysts.[101] Through an interplay of oxygen vacancies and the oxidation mechanism of organic sacrificial agents, initially high H_2 evolution rates are reduced by the deactivation of the catalyst eventually leading to a steady state activity, which, in the case of the presented work, is comparable among all three runs.

In addition, post-photocatalysis XRD analysis of the $n = 1$ oxide and oxyfluoride phases reveals changes in the diffraction patterns, indicating partial structural degradation under the applied photocatalytic conditions (Fig. S11a and b); this is in accordance with the decrease of photocatalytic activity observed for the $n = 1$ phase over time. In contrast, PXRD analysis of $n = 2$ oxide and oxyfluoride phases after photocatalytic H_2 evolution shows no detectable changes relative to the as-synthesized material, indicating higher structural stability of the double-layered RP framework under the applied aqueous photocatalytic conditions (Fig. S11c and d). This difference highlights the higher structural robustness of the $n = 2$ RP framework during aqueous photocatalytic operation. Furthermore, a more detailed analysis of the time-dependent behavior of the materials could help to understand the decomposition behavior and mechanism beyond the current state.

To analyse the charge carrier dynamics of the materials, transient absorption spectroscopy (TAS) measurements were conducted. The samples were excited with 355 nm laser light, and the dynamics of photogenerated charge carriers were recorded in the range from 760 nm to 950 nm. This detection area was chosen because, in chemically similar materials, photogenerated electrons appear in this wavelength range.[102–104]

In Fig. S12, the TAS maps of the four materials Sr_2TiO_4, $Sr_2TiO_3F_2$, $Sr_3Ti_2O_7$ and $Sr_3Ti_2O_5F_4$ are presented. One negative (here: laser scattering) and one positive signal (photogenerated electrons) could be observed. The intensities of the positive TAS signals differ in the samples and illustrate that the amount of photogenerated electrons in $Sr_3Ti_2O_7$ is the highest. This explains that $Sr_3Ti_2O_7$ is the best performing sample in the photocatalytic HER.

Regarding the other three sample (Sr_2TiO_4, $Sr_2TiO_3F_2$ and $Sr_3Ti_2O_5F_4$) the intensity of the TAS signals is not much different, meaning that the number of photogenerated electrons is comparable. Therefore, the lifetimes of the photogenerated electrons were analysed (Fig. S13 and Table S9). After fitting the decays, suitable lifetimes of the photogenerated electrons for the photocatalytic HER in all samples were achieved.[105] Comparing the samples with similar intensities of the TAS signals, Sr_2TiO_4, $Sr_2TiO_3F_2$ and $Sr_3Ti_2O_5F_4$, the values of the "baseline" are completely different. For $Sr_2TiO_3F_2$, the baseline is clearly increased in comparison to Sr_2TiO_4 and $Sr_3Ti_2O_5F_4$. Recently, we found that this increase in the baseline is beneficial for photocatalytic efficiency and indicates that very long-lived photoelectrons (lifetime ≫ 2.5 μs) are also involved in the photocatalytic HER. This observation is entirely consistent with the observed photocatalytic HER activity, as $Sr_2TiO_3F_2$ is the second-best sample for the HER. Furthermore, these long-lived photoelectrons might be a result of better charge separation due to internal dipole fields. Thus, the poor photocatalytic performance of Sr_2TiO_4 and $Sr_3Ti_2O_5F_4$ can be explained on the one hand by the low amount of photogenerated electrons, and on the other hand by the absence of very long-lived photoelectrons.

4.6 Understanding the optical properties and photocatalytic performances *via* DFT calculations

The calculated partial densities of states (PDOSs) show that the band gap of Sr_2TiO_4 (2.03 eV) becomes wider after fluorination (2.32 eV), whereas that of $Sr_3Ti_2O_7$ (1.95 eV) becomes narrower (1.62 eV) (Fig. 11); this is in general agreement with the experimentally observed band gap changes (see Fig. 6). Despite the known tendency of the PBE-GGA method to underestimate band gaps, the obtained results go against the general

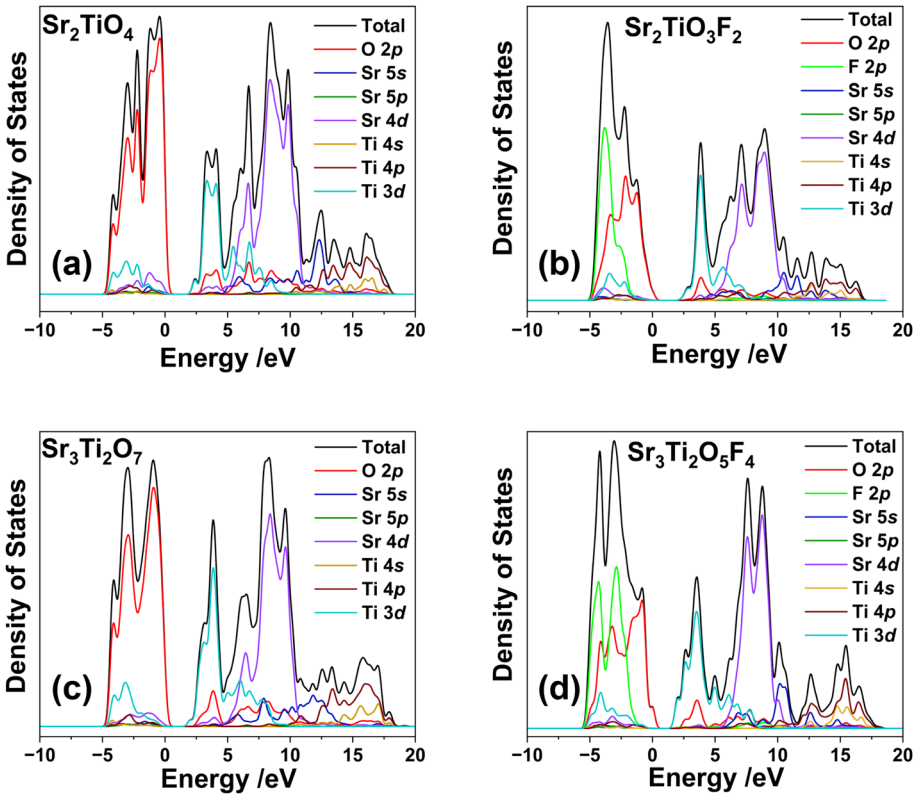

Fig. 11 PDOSs per-ion from DFT calculations for (a) Sr_2TiO_4, (b) $Sr_2TiO_3F_2$, (c) $Sr_3Ti_2O_7$, and (d) $Sr_3Ti_2O_5F_4$ ($E_f = 0$ eV).

expectation that the introduction of more electronegative F (3.98), compared to O (3.44), would lower the band center of the O/F-2p states at the VBM, thereby increasing the band gap. For all four phases, the VBM is mainly composed of O 2p states with a small contribution from Sr 4d orbitals, while the CBM is dominated by Ti 3d (t_{2g}-like) states (Fig. 11). Upon fluorination, F 2p states reside deeper in the valence manifold and do not create mid-gap states, consistent with the clean absorption onsets seen in UV-Vis DRS (Fig. 6). One clear change of VBM after fluorination is that the Sr 4d component shifts to a deeper energy region near the F 2p orbital (Fig. 11b and d). This is because the strong local electric field generated by F^-, resulting from its high electronegativity that attracts electron density, lowers the potential energy of nearby Sr orbitals. In addition, the strong electronegativity of F attracts more electron density from Sr, reducing the orbital hybridization between Sr and O on the opposite side. This leads to a more localized electron distribution on the equatorial O orbitals, which dominate the VBM of $Sr_2TiO_3F_2$ and $Sr_3Ti_2O_5F_4$ (Fig. 11b, d and SI S14). Together with the deeper energy level of newly introduced F that lowers the band center of the O/F-2p manifold, the VBM position shifts to a lower level, which is consistent with the UV-Vis-DRS results.

For the CBM, $Sr_3Ti_2O_5F_4$ exhibits a lower energy level, which narrows the band gap, whereas $Sr_2TiO_3F_2$ does not show such a tendency. In $Sr_2TiO_3F_2$, Ti is off-centered toward the apical oxygen (Fig. 5b), possibly due to the stronger electronic attraction of O^{2-} compared to F^-, which is structurally facilitated by the asymmetric filling of interstitial sites around the Ti coordination environment (every second layer filled, see Fig. 5). This displacement enhances the orbital hybridization between Ti $3d_{x^2-z^2}$ and O 2p orbitals, thereby maintaining the antibonding state at a higher energy level in the CBM. In contrast, Ti off-centering is negligible in $Sr_3Ti_2O_5F_4$ (again see Fig. 5) and consequently, the Ti 3d – O 2p hybridization becomes weaker compared to $Sr_2TiO_3F_2$, leading to a lower antibonding state in the CBM and a smaller band gap. This scenario is supported by the XPS measurements (Fig. 9a and c), where the Ti 2p peak shifts to higher binding energy due to the strong electron-withdrawing effect of F, which reduces the electron density around Ti. As a result, the orbital hybridization between Ti and the apical O becomes weaker, leading to electron localization on the apical oxygen and an increase in its electron density, which in turn causes the O 1s peak to shift to lower binding energy.

This deeper valence and modest upward shift of the conduction edge account for the limited changes in E_g. The +0.45 eV Ti 2p chemical shift in $Sr_3Ti_2O_5F_4$ is consistent with a more electronegative ligand field and a more regular apical coordination after fluorination; both effects increase the local electrostatic potential at Ti, in agreement with XPS results (Fig. 9). Butler–Ginley estimates based on the UV-Vis DRS gaps show that fluorination moves the CB to less-negative potentials and the VB to more-positive potentials for both $n = 1$ and 2 oxides and oxyfluorides (Fig. 7, Tables S6 and S7). The DFT results show a deeper valence, a slight upward shift of the conduction-band edge, and reduced c-axis dispersion, which

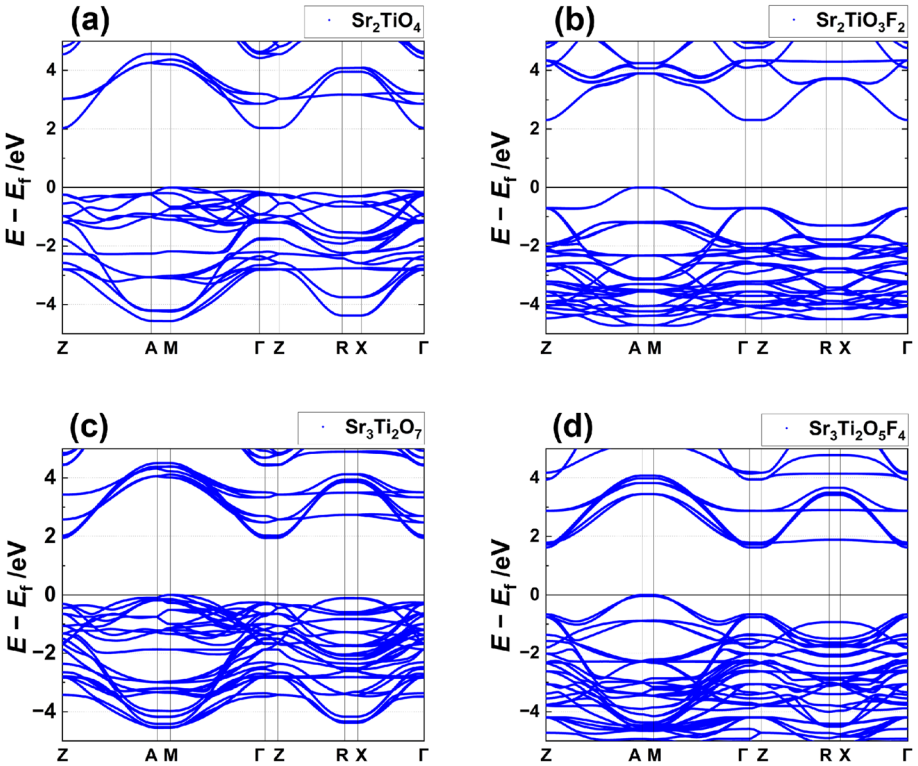

Fig. 12 Computed band structures of (a) Sr_2TiO_4, (b) $Sr_2TiO_3F_2$, (c) $Sr_3Ti_2O_7$, and (d) $Sr_3Ti_2O_5F_4$.

together provide the microscopic basis for these semi-empirical shifts. Consequently, $Sr_2TiO_3F_2$ retains sufficient CB driving force and gains polarity-assisted charge separation.

The computed band structures are shown in Fig. 12. All four phases exhibit indirect gaps: with conduction-band minimum at Γ and the valence-band maximum at M. The VBM for both fluorinated phases shows less orbital hybridization, which is due to the localized electrons in the O 2p orbitals discussed above. For the CBM, the in-plane dispersion from Γ to X (and Γ to M) remains similar across oxides and oxyfluorides, whereas fluorination flattens the branches from Γ to Z, indicating weaker interlayer coupling and reduced transport along the c-axis.

To assess the reliability of the PBE-derived bandgap trends, additional hybrid-functional (HSE06) calculations were performed for the $n = 1$ RP phases Sr_2TiO_4 and $Sr_2TiO_3F_2$ (please see SI Fig. S15). While the absolute band gaps increase relative to PBE, the fluorinated phase retains a wider band gap than the parent oxide, confirming that the qualitative bandgap widening upon fluorination is robust with respect to the choice of exchange–correlation functional (Table 2).

In order to learn the photoexcited electron mobility for the photocatalytic H_2 reaction, the directional electron effective masses were calculated by fitting the DFT band dispersion $E(k)$ in a small neighbourhood of the CBM (Fig. 13). The carrier mobility is inversely proportional to the effective mass; thus, a larger effective mass corresponds to lower mobility along that direction. For Sr_2TiO_4 and $Sr_3Ti_2O_7$, the in-plane effective mass is smaller than that along the out-of-plane direction, reflecting their layered perovskite nature. Upon fluorination, this anisotropy becomes more pronounced, with the in-plane to out-of-plane mobility ratio increasing to approximately 80 and 50 for $Sr_2TiO_3F_2$ and $Sr_3Ti_2O_5F_4$, respectively. This is attributed to the introduction of F at the apical sites, which forms strong ionic bonds and consequently reduces orbital hybridization with Ti 3d states along the c-axis. More interestingly, the double-layered perovskites $Sr_3Ti_2O_7$ and $Sr_3Ti_2O_5F_4$ exhibit almost the same in-plane effective mass, whereas only the out-of-plane effective mass shows a significant change after fluorination. This suggests that fluorine incorporation can reduce the conduction dimensionality while preserving the original in-plane conduction state.

Dimensional reduction in carrier mobility induced by an anisotropic anion environment has been reported for electronic transport in mixed-anion compounds.[32,106,107] For example, $SrVO_2H$, where the hydride H^- anions act as π-blockers along

Table 2 DFT (PBE) band extrema and directional electron effective masses, extracted from band curvatures along in-plane (Γ–X) and out-of-plane (Γ–Z) curvatures, respectively. E_g is the fundamental band gap and m_0 is the mass of free electrons

				Effective Mass (m_0)	
Compound	CBM	VBM	E_g (eV)	In-plane	Out-of-plane
Sr_2TiO_4	Γ	M	2.03	0.35	4.81
$Sr_2TiO_3F_2$	Γ	M	2.32	0.52	43.34
$Sr_3Ti_2O_7$	Γ	M	1.95	0.39	1.46
$Sr_3Ti_2O_5F_4$	Γ	M	1.62	0.39	21.50

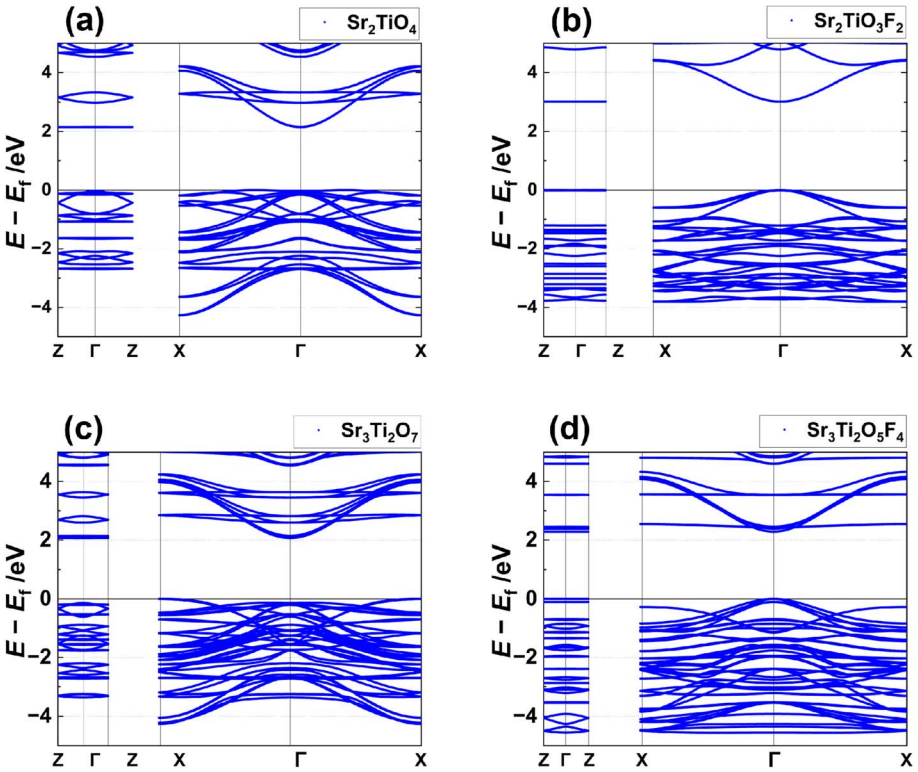

Fig. 13 Calculated effective masses: (a) Sr_2TiO_4, (b) $Sr_2TiO_3F_2$, (c) $Sr_3Ti_2O_7$, and (d) $Sr_3Ti_2O_5F_4$.

the *c*-axis, limits $V_{d\pi}$–H_{1s}–$V_{d\pi}$ coupling and thereby suppresses out-of-plane electronic dispersion. Thus, conduction is dominated by the in-plane V–O–V π network rather than along the *c* direction. In comparison, our effective-mass calculations reveal, for the first time, a similar anisotropic behavior expected for photoexcited carriers, opening up opportunities for photoexcited-carrier engineering through mixed-anion design strategies.

According to the DFT calculations, $Sr_2TiO_3F_2$ is expected to exhibit lower H_2 evolution activity than Sr_2TiO_4, since it possesses a wider band gap and lower carrier mobility in both the in-plane and out-of-plane directions. However, the experimental results contradict with this. One possible reason is the local polarity of the TiO_5F perovskite in $Sr_2TiO_3F_2$, which could enhance charge separation and dominate over reduced *c*-axis transport.[49] Since the off-centre shift is already present in $Sr_3Ti_2O_7$ due to the non-centrosymmetric site symmetry of Ti, and fluorination to $Sr_3Ti_2O_5F_4$ even leads to the absence of a clear off-centre shift, this polarity influence on the photocatalytic activity would not be expected for the $n = 2$ RP-type phases. Thus, this results in a less-negative conduction band together with heavier out-of-plane effective mass and correlates with the diminished activity. Thus, band alignment and local polar motifs, rather than surface area, govern the photocatalytic trends observed in these RP-type oxides and oxyfluorides. This atomistic picture is consistent with the observed ≈6.3-fold increase in the H_2 evolution rate compared to Sr_2TiO_4. In contrast, $Sr_3Ti_2O_5F_4$ has a CB that is too high in energy and thus might exhibit reduced out-of-plane transport, which would explain the suppressed H_2 evolution relative to $Sr_3Ti_2O_7$.

5 Conclusions

In this work, we investigated the structural, optical, and photocatalytic properties of the $n = 1$ and 2 RP-type titanates, Sr_2TiO_4 and $Sr_3Ti_2O_7$, together with their oxyfluorides, $Sr_2TiO_3F_2$ and $Sr_3Ti_2O_5F_4$. Our results show that fluorination in the $n = 1$ phase breaks inversion symmetry through apical O^{2-} with F^- substitution, producing asymmetric TiO_5F units that markedly enhance H_2 evolution, giving ~6.3-fold higher photocatalytic activity than the parent oxide. In contrast, the $n = 2$ homologue retains the space group symmetry and even lowers the local polar moment around the Ti cations after fluorination, and $Sr_3Ti_2O_5F_4$ exhibits largely reduced activity compared to $Sr_3Ti_2O_7$ despite comparable band gaps. XPS measurements support these structural assignments and are consistent with the more centrosymmetric coordination obtained from XRD. TAS provides direct photophysical insight into the charge-carrier dynamics across the series. $Sr_3Ti_2O_7$ exhibits the highest population of photogenerated electrons, consistent with its superior photocatalytic hydrogen evolution activity, while $Sr_2TiO_3F_2$ shows an enhanced long-lived electron component, indicating improved charge separation that correlates with its intermediate performance. In contrast, Sr_2TiO_4 and $Sr_3Ti_2O_5F_4$ display both lower effective electron populations and an absence of very long-lived carriers, consistent with their poor photocatalytic activity. DFT PDOS/band structures are

consistent with this interpretation, indicating a deeper valence band, a slight upward shift of the conduction edge, and reduced *c*-axis dispersion upon fluorination, in line with the Butler–Ginley band-edge trends and the opposite catalytic responses of the two *n*-series. Post-photocatalysis PXRD further reveals that the $n = 2$ RP crystal framework exhibits higher structural robustness under aqueous irradiation conditions, whereas partial degradation is observed for $n = 1$ oxide and oxyfluoride phases.

Overall, these findings demonstrate that while increasing *n* improves the intrinsic activity of the oxide series, fluorination can provide an additional local symmetry- and charge-separation-driven boost in certain RP-type structural and compositional scenarios. The contrasting behaviours establish that RP layer thickness, inversion-symmetry breaking, and charge-carrier dynamics collectively dictate the photocatalytic response in Sr–Ti RP-oxyfluorides. This highlights anion sublattice engineering as a selective strategy to tune symmetry and photocatalytic functionality in layered perovskite oxyfluorides.

Notes

An unformatted pre-print of the present work was deposited on ChemRxiv (Cambridge Open Engage).[108]

Author contributions

SP conceived and developed the research within the framework of the DFG-funded project, synthesized the materials, performed the majority of the experimental measurements, analyzed the data, and wrote the manuscript. OC contributed valuable scientific discussions. KMR, AH, and RM performed the photocatalytic H_2 evolution experiments and contributed to the scientific discussion. TA assisted during the re-synthesis of the compounds. HMF measured, processed and analyzed the XPS data. MW contributed to the scientific discussion. SRK and PA measured the BET surface area. RL and GS performed SEM imaging. JT measured TAS, analyzed the data and contributed to writing this section. CZ performed the DFT calculations as well as wrote the DFT part in the manuscript. All coauthors provided feedback and contributed to the internal review of the manuscript.

Conflicts of interest

The authors declare no competing financial interest.

Data availability

The data that support the findings of this study are available within the article and its supplementary information (SI) file. Additional data are available from the corresponding author upon reasonable request. Supplementary information: additional PXRD data, Rietveld refinement details, and crystallographic tables for Sr_2TiO_4, $Sr_2TiO_3F_2$, $Sr_3Ti_2O_7$, and $Sr_3Ti_2O_5F_4$, along with comparative literature values and bond-length analyses. It also contains a schematic diagram of the photocatalytic test setup with a corresponding photograph of the laboratory setup, as well as figures of the lamp emission spectrum, control experiments, hydrated and aged phase PXRD patterns, UV-Vis Kubelka–Munk plots, and N_2 adsorption–desorption isotherms. Supplementary XPS spectra (C 1s calibration and Ti 2p fitted regions) are provided to illustrate chemical shifts upon fluorination. Semi-empirical band-edge positions estimated via the Butler–Ginley method, TAS measurements, BET surface areas, and photocatalytic H_2 evolution data are summarized in accompanying tables. Furthermore, hybrid-functional (HSE06) electronic band structures for the $n = 1$ RP phases Sr_2TiO_4 and $Sr_2TiO_3F_2$ are provided. It also includes photocatalytic reproducibility tests of H_2 evolution for the most active sample, $Sr_3Ti_2O_7$, and post-photocatalytic PXRD patterns compared with corresponding as synthesized samples to evaluate the phase stability results. Partial densities of states of the O 2p orbitals, all references, energy parameters, and comparison data used for the band alignment calculations are also provided. See DOI: https://doi.org/10.1039/d5ta08602g.

Acknowledgements

This research project was financially supported by the German Research Foundation (DFG) funding within project number 518952364. OC, HMF, MW, and JPH acknowledge support from the collaborative research center FLAIR (Fermi level engineering applied to oxide electroceramics), which is funded by the German Research Foundation (DFG) (Project-ID No. 463184206-SFB 1548, subprojects: A05, Z02, A03/A04). SP acknowledges support from SFB 1548 FLAIR and discussions of defect-related concepts therein by becoming an associate member. SP thanks Dr Shravan Ravishankar Kousik (University of Stuttgart, Institute of Materials Science, Bioinspired Materials, Heisenbergstraβe 3, 70569 Stuttgart, Germany) for assisting during BET surface area measurements. SP thanks MSc. Benjamin Knies for assisting in DRS measurements, and Prof. Dr Biprajit Sarkar for the DRS facility access (University of Stuttgart, Institute of Inorganic Chemistry, Pfaffenwaldring 55, 70569 Stuttgart, Germany).

References

1 V. Balzani, L. Moggi, M. F. Manfrin, F. Bolletta and M. Gleria, Solar Energy Conversion by Water Photodissociation, *Science*, 1975, **189**, 852–856, DOI: 10.1126/science.189.4206.852.
2 G. T. Chavan, D. P. Dubal, E. C. Cho, D. R. Patil, J. S. Gwag, R. K. Mishra, Y. K. Mishra, J. An and J. Yi, A Roadmap of Sustainable Hydrogen Production and Storage: Innovations and Challenges, *Small*, 2025, **21**, 2411444, DOI: 10.1002/smll.202411444.
3 R. Marschall, 50 Years of Materials Research for Photocatalytic Water Splitting, *Eur. J. Inorg. Chem.*, 2021, **2021**, 2435–2441, DOI: 10.1002/ejic.202100264.
4 K. Obata, T. Higash, F. Ye, M. Katayama and K. Takanabe, Cation-Doped $SrTaO_2N$ Prepared through a Flux Method

for Visible-Light-Driven Water Splitting, *ChemPhotoChem*, 2023, **7**, e202200293, DOI: 10.1002/cptc.202200293.

5 Z. Qiao, Z. Liu, M. Ruan, Z. Guo, W. Yan and X. Wu, Thermal Excitation Polarized Field Drives Photoelectric Catalysis for Dye Degradation in a $BaTiO_3$/CdS Heterojunction through Integration of Solar and Thermal Energy, *ChemPhotoChem*, 2021, **5**, 1106–1118, DOI: 10.1002/cptc.202100176.

6 T. Rath, M. Deitermann, G. Zhao, G. W. Busser, H. Jansen, P. Schwiderowski, W. Xia and M. Muhler, Photocatalytic Deacon Reaction over $SrTiO_3$, *ChemPhotoChem*, 2021, **5**, 521–525, DOI: 10.1002/cptc.202000314.

7 M. Passi and B. Pal, A review on $CaTiO_3$ photocatalyst: Activity enhancement methods and photocatalytic applications, *Powder Technol.*, 2021, **388**, 274–304, DOI: 10.1016/j.powtec.2021.04.056.

8 A. Fujishima and K. Honda, Electrochemical Photolysis of Water at a Semiconductor Electrode, *Nature*, 1972, **238**, 37–38, DOI: 10.1038/238037a0.

9 P. A. DeSario, J. J. Pietron, D. H. Taffa, R. Compton, S. Schünemann, R. Marschall, T. H. Brintlinger, R. M. Stroud, M. Wark, J. C. Owrutsky, *et al.*, Correlating Changes in Electron Lifetime and Mobility on Photocatalytic Activity at Network-Modified TiO_2 Aerogels, *J. Phys. Chem. C*, 2015, **119**, 17529–17538, DOI: 10.1021/acs.jpcc.5b04013.

10 L. Schumacher, J. Timm and R. Marschall, Effects of hydrothermal etching and conversion on photocatalytic hydrogen evolution and overall water splitting with nanoparticulate and mesoporous TiO_2 and $SrTiO_3$/TiO_2 composites, *J. Mater. Chem. A*, 2024, **12**, 30768–30782, DOI: 10.1039/d4ta03416c.

11 H. Xiao, P. Liu, W. Wang, R. Ran, W. Zhou and Z. Shao, Ruddlesden–Popper Perovskite Oxides for Photocatalysis-Based Water Splitting and Wastewater Treatment, *Energy Fuels*, 2020, **34**(8), 9208–9221, DOI: 10.1021/acs.energyfuels.0c02301.

12 I. A. Rodionov, O. I. Silyukov, T. D. Utkina, M. V. Chislov, Y. P. Sokolova and I. A. Zvereva, Photocatalytic Properties and Hydration of Perovskite-Type Layered Titanates $A_2Ln_2Ti_3O_{10}$ (A = Li, Na, K; Ln = La, Nd), *Russ. J. Gen. Chem.*, 2012, **82**, 1191–1196, DOI: 10.1134/S1070363212070018.

13 I. A. Rodionov and I. A. Zvereva, Photocatalytic activity of layered perovskite-like oxides in practically valuable chemical reactions, *Russ. Chem. Rev.*, 2016, **85**(3), 248–279, DOI: 10.1070/RCR4547.

14 N. C. Hildebrandt, J. Soldat and R. Marschall, Layered Perovskite Nanofibers via Electrospinning for Overall Water Splitting, *Small*, 2015, **11**(17), 2051–2057, DOI: 10.1002/smll.201402679.

15 S. N. Ruddlesden and P. Popper, New compounds of the K_2NiF_4 type, *Acta Crystallogr.*, 1957, **10**, 538, DOI: 10.1107/S0365110X57001929.

16 B. V. Beznosikov and K. S. Aleksandrov, Perovskite-Like Crystals of the Ruddlesden–Popper Series, *Crystallogr. Rep.*, 2000, **45**, 792–798, DOI: 10.1134/1.1312923.

17 P. Wang, L. Liao, H. Chu, Y. Xie, Z. Li and W. Zhou, Recent Advances in Ruddlesden–Popper Phase-Layered Perovskite Sr_2TiO_4 Photocatalysts, *Nanomaterials*, 2025, **15**, 20, DOI: 10.3390/nano15010020.

18 J. He, X. Han, H. Xiang, R. Ran, W. Wang, W. Zhou and Z. Shao, Aluminum Cation Doping in Ruddlesden-Popper Sr_2TiO_4 Enables High-Performance Photocatalytic Hydrogen Evolution, *Hydrogen*, 2022, **3**, 501–511, DOI: 10.3390/hydrogen3040032.

19 B. S. Kwak, J. Y. Do, N. K. Park and M. Kang, Surface modification of layered perovskite Sr_2TiO_4 for improved CO_2 photoreduction with H_2O to CH_4, *Sci. Rep.*, 2017, **7**(1), 16370, DOI: 10.1038/s41598-017-16605-w.

20 J. Yu, J. Huang, R. Li, Y. Li, G. Liu and X. Xu, Fluorine-expedited nitridation of layered perovskite Sr_2TiO_4 for visible-light-driven photocatalytic overall water splitting, *Nat. Commun.*, 2025, **16**, 361, DOI: 10.1038/s41467-024-55748-z.

21 J. N. Yun, Z. Y. Zhang, J. F. Yan and W. Zhao, First-principles study of Sc-doping effect on the stability, electronic structure and photocatalytic properties of Sr_2TiO_4, *Thin Solid Films*, 2013, **542**, 276–280, DOI: 10.1016/j.tsf.2013.06.067.

22 H. Zhang, S. Ni, Y. L. Mi and X. X. Xu, Ruddlesden-Popper compound Sr_2TiO_4 co-doped with La and Fe for efficient photocatalytic hydrogen production, *J. Catal.*, 2018, **359**, 112–121, DOI: 10.1016/j.jcat.2017.12.031.

23 X. Sun and X. Xu, Efficient photocatalytic hydrogen production over La/Rh co-doped Ruddlesden-Popper compound Sr_2TiO_4, *Appl. Catal., B*, 2017, **210**, 149–159, DOI: 10.1016/j.apcatb.2017.03.063.

24 S. A. Kurnosenko, V. V. Voytovich, O. I. Silyukov, I. A. Rodionov and I. A. Zvereva, Photocatalytic Activity and Stability of Organically Modified Layered Perovskite-like Titanates $HLnTiO_4$ (Ln = La, Nd) in the Reaction of Hydrogen Evolution from Aqueous Methanol, *Catalysts*, 2023, **13**, 749, DOI: 10.3390/catal13040749.

25 M. A. Nowroozi, K. Wissel, J. Rohrer, A. R. Munnangi and O. Clemens, $LaSrMnO_4$: Reversible Electrochemical Intercalation of Fluoride Ions in the Context of Fluoride Ion Batteries, *Chem. Mater.*, 2017, **29**(8), 3441–3453, DOI: 10.1021/acs.chemmater.6b05075.

26 M. A. Nowroozi, S. Ivlev, J. Rohrer and O. Clemens, La_2CoO_4: a new intercalation based cathode material for fluoride ion batteries with improved cycling stability, *J. Mater. Chem. A*, 2018, **6**(11), 4658–4669, DOI: 10.1039/c7ta09427b.

27 A. Chen, X. Zhang, Z. Zhang, S. Yao and Z. Zhou, Band engineering of two-dimensional Ruddlesden–Popper perovskites for solar utilization: the relationship between chemical components and electronic properties, *J. Mater. Chem. A*, 2019, **7**, 11530–11536, DOI: 10.1039/c9ta01882d.

28 E. E. McCabe and C. Greaves, Fluorine insertion reactions into pre-formed metal oxides, *J. Fluorine Chem.*, 2007, **128**(4), 448–458, DOI: 10.1016/j.jfluchem.2006.11.008.

29 A. T. Giddings, E. A. S. Scott, M. C. Stennett, D. C. Apperley, C. Greaves, N. C. Hyatt and E. E. McCabe, Symmetry and the

Role of the Anion Sublattice in Aurivillius Oxyfluoride $Bi_2TiO_4F_2$, *Inorg. Chem.*, 2021, **60**, 14105–14115, DOI: 10.1021/acs.inorgchem.1c01933.

30 C. Bubeck, M. Widenmeyer, G. Richter, M. Coduri, E. Goering, S. Yoon and A. Weidenkaff, Tailoring of an unusual oxidation state in a lanthanum tantalum(IV) oxynitride via precursor microstructure design, *Commun. Chem.*, 2019, **2**, 134, DOI: 10.1038/s42004-019-0237-x.

31 M. Widenmeyer, J. Häcker, C. Bubeck, S. Yoon, O. Clemens and A. Weidenkaff, Sequential double anionic substitution through synthesis of perovskite-type $AB(O,N,F)_3$ with A = Ca, Sr, Ba and B = Ti, Zr, *Solid State Sci.*, 2023, **146**, 107376, DOI: 10.1016/j.solidstatesciences.2023.107376.

32 H. Kageyama, K. Hayashi, K. Maeda, J. P. Attfield, Z. Hiroi, J. M. Rondinelli and K. R. Poeppelmeier, Expanding frontiers in materials chemistry and physics with multiple anions, *Nat. Commun.*, 2018, **9**, 772, DOI: 10.1038/s41467-018-02838-4.

33 S. Perween, K. Wissel, Z. Dallos, M. Weiss, Y. Ikeda, S. Vasala, S. Strobel, P. Schützendübe, P. M. Jeschenko, U. Kolb, *et al.*, Topochemical Fluorination of $LaBaInO_4$ to $LaBaInO_3F_2$, Their Optical Characterization, and Photocatalytic Activities for Hydrogen Evolution, *Inorg. Chem.*, 2023, **62**, 16329–16342, DOI: 10.1021/acs.inorgchem.3c01682.

34 O. Clemens and P. R. Slater, Topochemical modifications of mixed metal oxide compounds by low-temperature fluorination routes, *Rev. Inorg. Chem.*, 2013, **33**(2–3), 105–117, DOI: 10.1515/revic-2013-0002.

35 X. Liu, Y. Zhang, C. Wang and L. Shen, Polar materials for photocatalytic applications: A critical review, *Interdiscip. Mater.*, 2024, **3**, 530–564, DOI: 10.1002/idm2.12176.

36 H. Suzuki, D. Ozaki, Y. Ishii, O. Tomita, D. Kato, H. Kageyama, S. Nozawa, K. Nakashima and R. Abe, A Sillén oxyhalide $SrBi_3O_4Cl_3$ as a promising photocatalyst for water splitting: impact of the asymmetric structure on light absorption and charge carrier dynamics, *J. Mater. Chem. A*, 2023, **11**, 15159–15167, DOI: 10.1039/d3ta00906h.

37 D. Kato, H. Suzuki, R. Abe and H. Kageyama, Band engineering of layered oxyhalide photocatalysts for visible-light water splitting, *Chem. Sci.*, 2024, **15**, 11719, DOI: 10.1039/d4sc02093f.

38 Y. Kobayashi, O. J. Hernandez, T. Sakaguchi, T. Yajima, T. Roisnel, Y. Tsujimoto, M. Morita, Y. Noda, Y. Mogami, A. Kitada, *et al.*, An oxyhydride of $BaTiO_3$ exhibiting hydride exchange and electronic conductivity, *Nat. Mater.*, 2012, **11**, 507–511, DOI: 10.1038/nmat3302.

39 Y. Chiba, K. Shibata, H. Takatsu, K. Fujii, M. Saito, H. Kageyama, K. Maeda, M. Yashima and T. Motohashi, Electrochemical Crystal Growth of Titanium Oxyfluorides - A Strategy for Development of Electron-Doped Materials, *Inorg. Chem.*, 2021, **60**, 14613–14621, DOI: 10.1021/acs.inorgchem.1c01640.

40 S. Guo, N. Tian, F. Chen, Y. Zhang and H. Huang, Layered perovskite $Bi_7Fe_2Ti_2O_{17}Cl$: Universally efficient photo-piezocatalysis and mechanismic insight into the origin of polarity, *Appl. Surf. Sci.*, 2025, **708**, 163661, DOI: 10.1016/j.apsusc.2025.163661.

41 Y. Tsujimoto, K. Yamaura and E. Takayama-Muromachi, Oxyfluoride Chemistry of Layered Perovskite Compounds, *Appl. Sci.*, 2012, **2**, 206–219, DOI: 10.3390/app2010206.

42 R. Kuriki, T. Ichibha, K. Hongo, D. Lu, R. Maezono, H. Kageyama, O. Ishitani, K. Oka and K. Maeda, A Stable, Narrow-Gap Oxyfluoride Photocatalyst for Visible-Light Hydrogen Evolution and Carbon Dioxide Reduction, *J. Am. Chem. Soc.*, 2018, **140**, 6648–6655, DOI: 10.1021/jacs.8b02822.

43 J. Jacobs, H.-C. Wang, M. A. L. Marques and S. G. Ebbinghaus, Ruddlesden–Popper Oxyfluorides $La_2Ni_{1-x}Cu_xO_3F_2$ ($0 \leq x \leq 1$): Impact of the Ni/Cu Ratio on the Thermal Stability and Magnetic Properties, *Inorg. Chem.*, 2024, **63**, 11317–11324, DOI: 10.1021/acs.inorgchem.4c01330.

44 J. Jacobs, J. R. Hester and S. G. Ebbinghaus, Cuprate Oxyfluorides $La_2Cu_{0.8}Ni_{0.2}O_3F_2$ and $La_2CuO_3F_2$ with "Channel-like" Anion Ordering, *Inorg. Chem.*, 2022, **61**, 17202–17211, DOI: 10.1021/acs.inorgchem.2c02776.

45 J. Jacobs, M. A. L. Marques, H.-C. Wang, E. Dieterich and S. G. Ebbinghaus, Structure, Magnetism, and Thermal Stability of $La_2NiO_{2.5}F_3$: A Ruddlesden–Popper Oxyfluoride Crystallizing in Space Group $P4_2/nnm$, *Inorg. Chem.*, 2021, **60**, 13646–13657, DOI: 10.1021/acs.inorgchem.1c01957.

46 S. Perween, B. Knies, M. Barroso, K. Wissel, R. Löser, C. Das, M. Saliba, O. Bondarchuk, H. Yilmaz and G. Schmitz, Anion Exchange in $LaBaInO_3F_2$: Structural and Optical Effects of Low-Temperature Topochemical Modification, *Inorg. Chem.*, 2026, **65**(5), 2728–2744, DOI: 10.1021/acs.inorgchem.5c03739.

47 O. Clemens, R. Kruk, E. A. Patterson, C. Loho, C. Reitz, A. J. Wright, K. S. Knight, H. Hahn and P. R. Slater, Introducing a Large Polar Tetragonal Distortion into Ba-Doped $BiFeO_3$ by Low-Temperature Fluorination, *Inorg. Chem.*, 2014, **53**, 12572–12583, DOI: 10.1021/ic502183t.

48 A. Vijay, K. Bairagi and S. Vaidya, Relating the structure, properties, and activities of nanostructured $SrTiO_3$ and $SrO–(SrTiO_3)n$ (n = 1 and 2) for photocatalytic hydrogen evolution, *Mater. Adv.*, 2022, **3**, 5055, DOI: 10.1039/d2ma00097k.

49 J. Yu and X. Xu, Fluorination over Cr doped layered perovskite Sr_2TiO_4 for efficient photocatalytic hydrogen production under visible light illumination, *J. Energy Chem.*, 2020, **51**, 30–38, DOI: 10.1016/j.jechem.2020.03.025.

50 H. Jeong, T. Kim, D. Kim and K. Kim, Hydrogen production by the photocatalytic overall water splitting on NiO/$Sr_3Ti_2O_7$: Effect of preparation method, *Int. J. Hydrogen Energy*, 2006, **31**, 1142–1146, DOI: 10.1016/j.ijhydene.2005.10.005.

51 K. Wissel, S. Dasgupta, A. Benes, R. Schoch, M. Bauer, R. Witte, A. D. Fortes, E. Erdem, J. Rohrer and O. Clemens, Developing intercalation based anode materials for fluoride-ion batteries: topochemical reduction of $Sr_2TiO_3F_2$ via a hydride based defluorination

process, *J. Mater. Chem. A*, 2018, **6**, 22013–22026, DOI: 10.1039/c8ta01012a.

52 K. Wissel, T. Vogel, S. Dasgupta, A. D. Fortes, P. R. Slater and O. Clemens, Topochemical Fluorination of $n = 2$ Ruddlesden–Popper Type $Sr_3Ti_2O_7$ to $Sr_3Ti_2O_5F_4$ and Its Reductive Defluorination, *Inorg. Chem.*, 2020, **59**, 1153–1163, DOI: 10.1021/acs.inorgchem.9b02783.

53 P. R. Slater and R. K. B. Gover, Synthesis and structure of the new oxide fluoride $Sr_2TiO_3F_2$ from the low temperature fluorination of Sr_2TiO_4: an example of a staged fluorine substitution/insertion reaction, *J. Mater. Chem.*, 2002, **12**, 291–294, DOI: 10.1039/b106574m.

54 P. R. Slater, Poly(vinylidene Fluoride) as a reagent for the synthesis of K_2NiF_4-related inorganic oxide Fluorides, *J. Fluorine Chem.*, 2002, **117**, 43–45, DOI: 10.1016/S0022-1139(02)00166-5.

55 Bruker, *Diffrac.SUITE TOPAS V.6.0*. 2017.

56 J. Perl, J. Shin, J. Schümann, B. Faddegon and H. Paganetti, TOPAS: An innovative proton Monte Carlo platform for research and clinical applications, *Med. Phys.*, 2012, **39**(11), 6818–6837, DOI: 10.1118/1.4758060.

57 A. E. Morales, E. S. Mora and U. Pal, Use of diffuse reflectance spectroscopy for optical characterization of un-supported nanostructures, *Rev. Mex. Fis. S*, 2007, **53**(3), 18–22.

58 R. W. Frei and J. D. MacNeil, *Diffuse Reflectance Spectroscopy in Environmental Problem-Solving*, CRC Press, 1973, DOI: 10.1201/9781351071413.

59 A. Walsh and K. T. Butler, Prediction of Electron Energies in Metal Oxides, *Acc. Chem. Res.*, 2014, **47**(2), 364–372, DOI: 10.1021/ar400115x.

60 M. A. Butler and D. S. Ginley, Prediction of Flatband Potentials at Semiconductor-Electrolyte Interfaces from Atomic Electronegativities, *J. Electrochem. Soc.*, 1978, **125**(2), 228–232, DOI: 10.1149/1.2131419.

61 F. E. Halouani and A. Deschanvres, Interfaces semi-conducteur-electrolyte: Correlations entre le potentiel de bande plate et les echelles d'electronegativite, *Mater. Res. Bull.*, 1982, **17**(8), 1045–1052, DOI: 10.1016/0025-5408(82)90130-1.

62 H. Arthur and J. Nethercot, Prediction of Fermi Energies and Photoelectric Thresholds Based on Electronegativity Concepts, *Phys. Rev. Lett.*, 1974, **33**, 1088, DOI: 10.1103/PhysRevLett.33.1088.

63 A. Kramida, Y. Ralchenko, J. Reader and NIST ASD Team, *NIST Atomic Spectra Database (ver. 5.12)*, National Institute of Standards and Technology, Gaithersburg, MD, 2024, DOI: 10.18434/T4W30F, available online https://physics.nist.gov/asd, accessed 22 September 2025.

64 R. D. Johnson III, NIST Computational Chemistry Comparison and Benchmark Database, *NIST Standard Reference Database Number 101*, 2022, https://cccbdb.nist.gov//, accessed 22 September 2025.

65 R. S. Mulliken, A New Electroaffinity Scale; Together with Data on Valence States and on Valence Ionization Potentials and Electron Affinities, *J. Chem. Phys.*, 1934, **2**, 782–793, DOI: 10.1063/1.1749394.

66 J. Gao, W. Zeng, R. Luo, Z. Liu and Q.-J. Liu, The Applicable Guideline for the Three Criteria in Identifying p/n-Type Characteristics, *Cryst. Growth Des.*, 2024, **24**, 3777–3785, DOI: 10.1021/acs.cgd.4c00108.

67 N. Fairley, V. Fernandez, M. Richard-Plouet, C. Guillot-Deudon, J. Walton, E. Smith, D. Flahaut, M. Greiner, M. Biesinger, S. Tougaard, *et al.*, Systematic and collaborative approach to problem solving using X-ray photoelectron spectroscopy, *Appl. Surf. Sci. Adv.*, 2021, **5**, 100112, DOI: 10.1016/j.apsadv.2021.100112.

68 J. H. Scofield, Hartree-Slater subshell photoionization cross-sections at 1254 and 1487 eV, *J. Electron Spectrosc. Relat. Phenom.*, 1976, **8**(2), 129–137, DOI: 10.1016/0368-2048(76)80015-1.

69 S. J. Clark, M. D. Segall, C. J. Pickard, P. J. Hasnip, M. I. J. Probert, K. Refson and M. C. Payne, First principles methods using CASTEP, *Z. Kristallogr.*, 2005, **220**, 567–570, DOI: 10.1524/zkri.220.5.567.65075.

70 J. P. Perdew, K. Burke and M. Ernzerhof, Generalized Gradient Approximation Made Simple, *Phys. Rev. Lett.*, 1996, **77**, 3865–3868, DOI: 10.1103/PhysRevLett.77.3865.

71 H. J. Monkhorst and J. D. Pack, Special points for Brillouin-zone integrations, *Phys. Rev. B*, 1976, **13**(12), 5188–5192, DOI: 10.1103/PhysRevB.13.5188.

72 K. Hummer, J. Harl and G. Kresse, Heyd-Scuseria-Ernzerhof hybrid functional for calculating the lattice dynamics of semiconductors, *Phys. Rev. B*, 2009, **80**, 115205, DOI: 10.1103/PhysRevB.80.115205.

73 J. Heyd; and G. E. Scuseria, Efficient hybrid density functional calculations in solids: Assessment of the Heyd–Scuseria–Ernzerhof screened Coulomb hybrid functional, *J. Chem. Phys.*, 2004, **121**, 1187, DOI: 10.1063/1.1760074.

74 P. Y. Yu and M. Cardona, *Fundamentals of Semiconductors*, Springer, 2010, DOI: 10.1007/978-3-642-00710-1.

75 G. K. H. Madsen, J. Carrete and M. J. Verstraete, BoltzTraP2, a program for interpolating band structures and calculating semi-classical transport coefficients, *Comput. Phys. Commun.*, 2018, **231**, 140–145, DOI: 10.1016/j.cpc.2018.05.010.

76 Y. Tsujimoto, K. Yamaura, N. Hayashi, K. Kodama, N. Igawa, Y. Matsushita, Y. Katsuya, Y. Shirako, M. Akaogi and E. Takayama-Muromachi, Topotactic Synthesis and Crystal Structure of a Highly Fluorinated Ruddlesden–Popper-Type Iron Oxide, $Sr_3Fe_2O_5{+}xF_{2-x}$ ($x \approx 0.44$), *Chem. Mater.*, 2011, **23**, 3652–3658, DOI: 10.1021/cm201075g.

77 N. N. M. Gurusinghe, J. C. Fones, J. F. Marco, F. J. Berry and C. Greaves, Fluorine insertion into the Ruddlesden–Popper phase $La_2BaFe_2O_7$: the structure and magnetic properties of $La_2BaFe_2O_5F_4$, *Dalton Trans.*, 2014, **43**, 2038–2043, DOI: 10.1039/c3dt52769g.

78 M. Ziati, N. Bekkioui and H. Ez-Zahraouy, Ruddlesden-Popper compound Sr_2TiO_4 doped with chalcogens for optoelectronic applications: Insights from first-principle calculations, *Chem. Phys.*, 2021, **548**, 111221, DOI: 10.1016/j.chemphys.2021.111221.

79 E. Pastor, M. Sachs, S. Selim, J. R. Durrant, A. A. Bakulin and A. Walsh, Electronic defects in metal oxide photocatalysts,

Nat. Rev. Mater., 2022, **7**, 503–521, DOI: 10.1038/s41578-022-00433-0.

80 K. v. Benthem, C. Elsässer and R. H. French, Bulk electronic structure of $SrTiO_3$: Experiment and theory, *J. Appl. Phys.*, 2001, **90**, 6156–6164, DOI: 10.1063/1.1415766.

81 W. Li, S. Niu, B. Zhao, R. Haiges, Z. Zhang, J. Ravichandran and A. Janotti, Band gap evolution in Ruddlesden-Popper phases, *Phys. Rev. Mater.*, 2019, **3**, 101601(R), DOI: 10.1103/PhysRevMaterials.3.101601.

82 M. Barroso, M. Dai, C. Bubeck, M. Scavini, G. J. Cuello, H. Zhang, A. Weidenkaff and M. Widenmeyer, Investigation of O/N Ordering in Perovskite-Type Oxynitrides $La_{1-x}Y_xTa(O,N)_3$ on Long Range and Short Scale, *Inorganics*, 2024, **12**, 90, DOI: 10.3390/inorganics12030090.

83 M. Tarek, F. Yasmeen and M. A. Basith, Nanostructured $DyFeO_3$ photocatalyst: an authentic and effective approach for remediation of industrial and pharmaceutical wastewater, *J. Mater. Chem. A*, 2024, **12**, 25475, DOI: 10.1039/d4ta04728a.

84 M. Tarek, F. Yasmeen and M. A. Basith, Mechanistic insights into the enhanced photocatalytic efficiency of MoS_2-tuned $DyFeO_3$ heterojunction nanocomposites for pollutant degradation, *Nanoscale*, 2025, **17**, 6620, DOI: 10.1039/d4nr05281a.

85 R. Haul, S. J. Gregg and K. S. W. Sing, Adsorption, Surface Area and Porosity, *2. Auflage, Academic Press, London 1982. 303 Seiten. Berichte der Bunsengesellschaft für physikalische Chemie*, 1982, **86**(10), 957, DOI: 10.1002/bbpc.19820861019.

86 M. C. Biesinger, L. W. M. Lau, A. R. Gerson and R. S. C. Smart, Resolving surface chemical states in XPS analysis of first row transition metals, oxides and hydroxides: Sc, Ti, V, Cu and Zn, *Appl. Surf. Sci.*, 2010, **257**, 887–898, DOI: 10.1016/j.apsusc.2010.07.086.

87 J. F. Moulder, W. F. Stickle, P. E. Sobol and K. D. Bomben, *Handbook of X-Ray Photoelectron Spectroscopy*, Perkin-Elmer Corporation, Physical Electronics Division, 1992.

88 A. V. Naumkin, A. Kraut-Vass, S. W. Gaarenstroom and C. J. Powell, *NIST X-Ray Photoelectron Spectroscopy Database (SRD 20), Version 5.0*, National Institute of Standards and Technology (NIST), available online https://srdata.nist.gov/xps/, accessed 22 September 2025.

89 M. Widenmeyer, T. Kohler, M. Samolis, A. T. D. Denko, X. Xiao, W. Xie, F. E. Osterloh and A. Weidenkaff, Band Gap Adjustment in Perovskite-type $Eu_{1-x}Ca_xTiO_3$ *via* Ammonolysis, *Z. Phys. Chem.*, 2020, **234**(5), 887–909, DOI: 10.1515/zpch-2019-1429.

90 B. D. Bhuskute, H. Ali-Löytty, J. Saari, A. Tukiainen and M. Valden, Ti^{3+} Self-Doping-Mediated Optimization of TiO_2 Photocatalyst Coating Grown by Atomic Layer Deposition, *ACS Appl. Eng. Mater.*, 2024, **2**, 2278–2284, DOI: 10.1021/acsaenm.4c00372.

91 Y. Wang, C. Qiu, Y. Xie, L. Wang, J. Ding, J. Zhang, H. Wan and G. Guan, Intentionally Introducing Oxygen Vacancies and Ti^{3+} Defects on the Surface of $Bi_4Ti_3O_{12}$ Nanosheets for Promoting the Photoreduction of CO_2 to CH_3OH, *ACS Appl. Nano Mater.*, 2024, **7**, 3012–3023, DOI: 10.1021/acsanm.3c05346.

92 A. Kudo and Y. Miseki, Heterogeneous photocatalyst materials for water splitting, *Chem. Soc. Rev.*, 2009, **38**(1), 253–278, DOI: 10.1039/b800489g.

93 H. L. B. Boström, M. S. Senn and A. L. Goodwin, Recipes for improper ferroelectricity in molecular perovskites, *Nat. Commun.*, 2018, **9**, 2380, DOI: 10.1038/s41467-018-04764-x.

94 A. Klein, K. Albe, N. Bein, O. Clemens, K. A. Creutz, P. Erhart, M. Frericks, E. Ghorbani, J. P. Hofmann, B. Huang, *et al.*, The Fermi energy as common parameter to describe charge compensation mechanisms: A path to Fermi level engineering of oxide electroceramics, *J. Electroceram.*, 2023, **51**, 147–177, DOI: 10.1007/s10832-023-00324-y.

95 Y. Chen, M. Cai, Y. Cao, S. S. A. Shuaib, J.-q. Bai, F. Chen, J. Xue, Y. Wei and S. Sun, Efficient photocatalytic water splitting using Sn-doped $SrTiO_3$ perovskite with Sn at Sr sites, *Catal. Sci. Technol.*, 2025, **15**, 3316–3324, DOI: 10.1039/d5cy00338e.

96 Y. Xu, Y. Liang, Q. He, R. Xu, D. Chen, X. Xu and H. Hu, Review of doping $SrTiO_3$ for photocatalytic applications, *Bull. Mater. Sci.*, 2023, **46**(6), DOI: 10.1007/s12034-022-02826-x.

97 K. Zhang, L.-C. Yin and G. Liu, Suppression of Ti^{3+} recombination centers in Ti-based metal oxide photocatalysts by Al doping, *Phys. Rev. B*, 2025, **111**, 075127, DOI: 10.1103/PhysRevB.111.075127.

98 D. Ozaki, H. Suzuki, K. Ogawa, R. Sakamoto, Y. Inaguma, K. Nakashim, O. Tomita, H. Kageyama and R. Abe, Synthesis, band structure and photocatalytic properties of Sillén–Aurivillius oxychlorides $BaBi_5Ti_3O_{14}Cl$, $Ba_2Bi5Ti_4O_{17}Cl$ and $Ba_3Bi_5Ti_5O_{20}Cl$ with triple-, quadruple- and quintuple-perovskite layers, *J. Mater. Chem. A*, 2021, **9**, 8332–8340, DOI: 10.1039/d0ta12550d.

99 J. Yu, W. Wang, B. Cheng and B.-L. Su, Enhancement of Photocatalytic Activity of Mesoporous TiO_2 Powders by Hydrothermal Surface Fluorination Treatment, *J. Phys. Chem. C*, 2009, **113**, 6743–6750, DOI: 10.1021/jp900136q.

100 S. Wang, B. Huang, Z. Wang, Y. Liu, W. Wei, X. Qin, X. Zhang and Y. Dai, A new photocatalyst: $Bi_2TiO_4F_2$ nanoflakes synthesized by a hydrothermal method, *Dalton Trans.*, 2011, **40**, 12670–12675, DOI: 10.1039/c1dt10889a.

101 G. M. Haselmann and D. Eder, Early-Stage Deactivation of Platinum-Loaded TiO_2 Using In Situ Photodeposition during Photocatalytic Hydrogen Evolution, *ACS Catal.*, 2017, **7**(7), 4668–4675, DOI: 10.1021/acscatal.7b00845.

102 L. Schumacher, J. Timm, A. Hofmann and R. Marschall, $SrTiO_3$ Sol–Gel Synthesis Enables Enhanced Photocatalytic Overall Water Splitting Activity by Al and/or Ga (co-)Doping and in-situ Formation of a $SrTiO_3/SrCO_3$ Heterojunction, *Artif. Photosynth.*, 2026, DOI: 10.1021/aps.5c00025.

103 A. Yamakata, J. J. M. Vequizo and M. Kawaguchi, Behavior and Energy State of Photogenerated Charge Carriers in Single-Crystalline and Polycrystalline Powder $SrTiO_3$ Studied by Time-Resolved Absorption Spectroscopy in the

Visible to MidInfrared Region, *J. Phys. Chem. C*, 2015, **119**, 1880–1885, DOI: 10.1021/jp510647b.

104 J. J. M. Vequizo, S. Nishioka, J. Hyodo, Y. Yamazaki, K. Maeda and A. Yamakata, Crucial impact of reduction on the photocarrier dynamics of $SrTiO_3$ powders studied by transient absorption spectroscopy, *J. Mater. Chem. A*, 2019, **7**, 26139–26146, DOI: 10.1039/c9ta08216f.

105 J. Ma, T. J. Miao and J. Tang, Charge carrier dynamics and reaction intermediates in heterogeneous photocatalysis by time-resolved spectroscopies, *Chem. Soc. Rev.*, 2022, **51**, 5777, DOI: 10.1039/d1cs01164b.

106 T. Yamamoto, D. Zeng, T. Kawakami, V. Arcisauskaite, K. Yata, M. A. Patino, N. Izumo, J. E. McGrady, H. Kageyama and M. A. Hayward, The role of π-blocking hydride ligands in a pressure-induced insulator-to-metal phase transition in $SrVO_2H$, *Nat. Commun.*, 2017, **8**, 1217, DOI: 10.1038/s41467-017-01301-0.

107 Q. D. Gibson, T. D. Manning, M. Zanella, T. Zhao, P. A. E. Murgatroyd, C. M. Robertson, L. A. H. Jones, F. McBride, R. Raval, F. Cora, *et al.*, Modular Design via Multiple Anion Chemistry of the High Mobility van der Waals Semiconductor $Bi_4O_4SeCl_2$, *J. Am. Chem. Soc.*, 2020, **142**, 847–856, DOI: 10.1021/jacs.9b09411.

108 S. Perween, K. M. Ries, A. Hofmann, T. Aalto, H. M. Fernández, M. Widenmeyer, R. Löser, G. Schmitz, P. Atanasova and J. P. Hofmann *et al.*, Structural origins of photocatalytic properties in Ruddlesden–Popper $Sr_{n+1}Ti_nO_{3n+1}$ $(n = 1, 2)$ and their topochemically fluorinated phases $Sr_{n+1}Ti_nO_{(3n+1)-x}F_{2x}$ $(x \approx n)$, *ChemRxiv*, Cambridge Open Engage, Cambridge, 2025.